

1 **Title**

2 Regulatory variants active in iPSC-derived pancreatic progenitor cells are associated with Type 2 Diabetes in  
3 adults

4 **Authors**

5 Jennifer P. Nguyen<sup>2,3,†</sup>, Agnieszka D’Antonio-Chronowska<sup>1,†</sup>, Kyohei Fujita<sup>1</sup>, Bianca M. Salgado<sup>4</sup>, Hiroko  
6 Matsui<sup>4</sup>, Timothy D. Arthur<sup>3,5</sup>, iPSCORE Consortium<sup>6</sup>, Margaret K.R. Donovan<sup>2,3</sup>, Matteo D’Antonio<sup>1</sup>, Kelly A.  
7 Frazer<sup>1,4,\*</sup>

8 **Affiliations:**

9 <sup>1</sup> Department of Pediatrics, University of California, San Diego, La Jolla, CA, 92093, USA

10 <sup>2</sup> Bioinformatics and Systems Biology Graduate Program, University of California, San Diego, La Jolla, CA,  
11 92093, USA

12 <sup>3</sup> Department of Biomedical Informatics, University of California, San Diego, La Jolla, CA, 92093, USA

13 <sup>4</sup> Institute of Genomic Medicine, University of California San Diego, 9500 Gilman Dr, La Jolla, CA, 92093, USA

14 <sup>5</sup> Biomedical Sciences Graduate Program, University of California, San Diego, La Jolla, CA 92093, USA

15 <sup>6</sup> A full list of Consortium members and their affiliations appears at the end of the manuscript

16 \* Correspondence to: Kelly A. Frazer; Tel: +1 (858) 246-0208; Email: [kafrazer@health.ucsd.edu](mailto:kafrazer@health.ucsd.edu).

17 † Equal contributions

## 18 **Abstract**

19 Pancreatic progenitor cells (PPC) are an early developmental multipotent cell type that give rise to mature  
20 endocrine, exocrine, and ductal cells. To investigate the extent to which regulatory variants active in PPC  
21 contribute to pancreatic complex traits and disease in the adult, we derived PPC from induced pluripotent stem  
22 cells (iPSCs) of nine unrelated individuals and generated single cell profiles of chromatin accessibility (snATAC-  
23 seq) and transcriptome (scRNA-seq). While iPSC-PPC differentiation was asynchronous and included cell types  
24 from early to late developmental stages, we found that the predominant cell type consisted of NKX6-1+  
25 progenitors. Genetic characterization using snATAC-seq identified 86,261 regulatory variants that either  
26 displayed chromatin allelic bias and/or were predicted to affect active transcription factor (TF) binding sites.  
27 Integration of these regulatory variants with 380 fine-mapped type 2 diabetes (T2D) risk loci identified regulatory  
28 variants in 209 of these loci that are functional in iPSC-PPC, either by affecting transcription factor binding or  
29 through association with allelic effects on chromatin accessibility. The PPC active regulatory variants in 65 of  
30 these loci showed strong evidence of causally underlying the association with T2D. Our study shows that studying  
31 the functional associations of regulatory variation in iPSC-PPC enables the identification and characterization of  
32 causal SNPs for adult Type 2 Diabetes.

## 33 **Introduction**

34 In early development the pancreas is formed from pancreatic progenitor cells (PPCs), which are a multipotent cell  
35 type that has the potential to give rise to endocrine cells (clusters of hormone secreting cells, such as  $\alpha$ ,  $\beta$ ,  $\gamma$ , and  $\delta$   
36 cells) and exocrine cells (i.e. acinar and ductal cells) (Cano et al., 2014; Jennings et al., 2015). While PPCs are  
37 precursors to mature pancreas cell types, the extent to which regulatory variants active in PPCs contribute to  
38 pancreatic complex traits and disease in the adult is currently not known. Recently it has become possible to use  
39 human pluripotent stem cells to derive PPCs (Pagliuca et al., 2014; Reznick et al., 2014), which provide a virtually  
40 unlimited source of cells to identify and characterize regulatory variants. Given that regulatory variation is largely  
41 located in enhancers and promoters (Pennacchio et al., 2013), ATAC-seq provides an optimal method to identify  
42 and characterize variants in PPCs that directly alter transcription factor binding and downstream gene expression.  
43 Examining induced pluripotent stem cell derived PPCs (iPSC-PPCs) from whole-genome sequenced unrelated  
44 individuals using ATAC-seq could enable identification of regulatory variation in PPCs and determine whether  
45 or not they are associated with adult pancreatic traits and diseases such as Type 2 Diabetes (T2D).

46 PPCs are characterized as a population of cells that have differentiated beyond the pancreatic foregut, committed  
47 to a pancreatic progenitor fate, and marked by the co-expression of *PDX1* and *NKX6-1* (Cano et al., 2014; Jennings  
48 et al., 2015). A reference set of embryonic stem cell-derived PPCs (ESC-PPC) obtained across multiple  
49 differentiation stages have shown the presence of multiple cell types, including pancreatic progenitors, endocrine  
50 cells and exocrine cells (Veres et al., 2019), suggesting that stem cell differentiation of PPCs is likely  
51 asynchronous. It is currently unclear how closely iPSC-PPC will be to ESC-PPC, i.e., whether similar cell types  
52 resulting from asynchronous differentiation will be observed. Furthermore, the reproducibility of pancreatic  
53 differentiation across iPSC lines derived from different individuals is unknown.

54

55 The development of single nuclear ATAC-seq (snATAC-seq) has become a powerful tool to investigate the  
56 mechanisms underlying the function of regulatory variants (Chiou et al., 2021; Rai et al., 2020). snATAC-seq  
57 pinpoints the locations of regulatory elements across the genome; and integration with motif footprinting and  
58 transcription factor binding prediction tools enable the identification of transcription factor binding sites  
59 associated with each snATAC-seq peak as well as a determination of the allelic effects of each SNP on  
60 transcription factor binding (Bentsen et al., 2020; Ghandi et al., 2014; Ghandi et al., 2016; Yan et al., 2021).  
61 Therefore, snATAC-seq provides an optimal approach to characterize regulatory genetic variation and to identify  
62 molecular mechanisms (i.e. transcription factor binding) underlying the associations between genotype and T2D.  
63 The genetic variants associated with the most common pancreatic disease, T2D, have been investigated in  
64 millions of people, resulting in the identification of more than 500 loci (Mahajan et al., 2018; Vujkovic et al.,  
65 2020). Although several studies have successfully identified the likely causal variant in a small subset of T2D-  
66 associated loci (Chiou et al., 2021; Mahajan et al., 2018; Varshney et al., 2017), the vast majority of the signals  
67 still remains uncharacterized and typically lie within regulatory regions. Given the importance of many  
68 transcription factors in regulating pancreatic cells' function, it is not surprising that many non-coding validated  
69 T2D risk variants overlap transcription factor binding sites (Chiou et al., 2021; Geusz et al., 2020; Greenwald et  
70 al., 2019; Mahajan et al., 2018; Rai et al., 2020; Thurner et al., 2018), indicating that snATAC-seq provides an  
71 optimal method to identify the molecular mechanisms underlying the role of regulatory variants in this disease.  
72 Here, we investigated the potential of iPSC-PPC as a model system to study the associations between genetic  
73 variation, gene regulation and T2D. We used nine iPSC lines from unrelated individuals (Panopoulos et al., 2017)  
74 and a 15-day differentiation protocol to obtain ten iPSC-PPC samples. We characterized these iPSC-PPC samples  
75 using scRNA-seq and snATAC-seq and found that, while differentiation occurs asynchronously across iPSC lines,  
76 the vast majority of derived cells are NKX6-1+ progenitors, which represent early pancreatic lineage to endocrine  
77 cells. We investigated the associations between genetic variation and the function of chromatin accessible regions

78 in iPSC-PPC and observed that 86,261 regulatory variants either overlapped footprints of transcription factors  
79 active in iPSC-PPC, were predicted to have allelic effects on transcription factor binding sites, and/or were  
80 demonstrated to have allelic-specific effects on snATAC-seq signals. We next investigated the overlap between  
81 these variants and SNPs included in 380 functional T2D credible sets from a recent GWAS (Mahajan et al., 2018)  
82 and found that 209 had SNPs that either overlapped binding sites of active transcription factors and/or were  
83 associated with allelic effects, including 65 that showed strong evidence of being causal. This study demonstrates  
84 that many T2D risk variants overlap regulatory elements active in iPSC-PPC and display allelic effects due to  
85 altered transcription factor binding, indicating that iPSC-PPC are a suitable model system to study the genetics  
86 of T2D in adults.

## 87 Results

88 We used iPSC lines from nine unrelated iPSCORE individuals (Panopoulos et al., 2017) ([Table S1](#)) and a 15-day  
89 differentiation protocol to derive ten iPSC-derived pancreatic progenitor (iPSC-PPC) samples (one iPSC clone  
90 was differentiated twice; [Figure 1A](#)). To perform a baseline assessment of iPSC-PPC differentiation efficiency,  
91 we measured the fraction of cells positive for two hallmark PPC transcription factors, PDX1 and NKX6-1, using  
92 flow cytometry, and observed that the ten samples differentiated with varying efficiency ([Figure S1](#)). The fraction  
93 of cells that stained positive for PDX1 ranged from 22.1 to 96.4%, and the fraction that was double-positive  
94 stained for PDX1 and NKX6-1 ranged from 9.4 to 91.7% ([Figure S1B](#)). As expression of NKX6-1 occurs later  
95 than PDX1 expression during development, the lower fraction of double-positive cells reflect asynchronous  
96 differentiation resulting in pancreatic progenitor cells at slightly different stages of maturity.

### 97 iPSC-PPC cell types characterized by scRNA-seq and snATAC-seq

98 To better understand the cellular heterogeneity of the iPSC-PPCs, we performed scRNA-seq on one iPSC clone  
99 and all ten iPSC-PPC samples (83,971 cells, 18,217 expressed genes), as well as snATAC-seq on seven of these  
100 samples (26,564 nuclei, 288,813 peaks). We integrated the scRNA-seq samples using Seurat (Butler et al., 2018)  
101 and detected eight distinct cell clusters ([Figure 1B,C](#), [Figure S2](#), [Figure S3](#), [Table S2](#)). We found that the majority  
102 of the cells belonged to one cluster (52,014 cells, 61.94%). This observation was also reflected in snATAC-seq  
103 where a large proportion of nuclei (24,560 nuclei, 92.46%) belonged to a single cluster despite the fewer number  
104 of clusters (five) detected in snATAC-seq ([Figure 1D,E](#), [Figure S4](#), [Table S4](#)).

105 To annotate each cell type in scRNA-seq, we compared the expression levels of marker genes in each of the eight  
106 clusters with the expression levels in eight pancreatic progenitor cell types over four different stages during  
107 embryonic stem cell differentiation in the ESC-PPC reference study ([Figure 1F](#), [Table S3](#)) (Veres et al., 2019).  
108 The Veres et al. study (Veres et al., 2019) included cell types corresponding to populations in the iPSC-PPCs

(PDX1+ progenitors, NKX6-1+ progenitors, endocrine cells, and non-endocrine cells) as well as advanced cells ( $\alpha$  and  $\beta$  cells) not represented in the iPSC-PPCs. For the cell types present in both studies, we identified clusters within the iPSC-PPCs that exhibit similar expression profiles as the corresponding cells in the ESC-PPCs: PDX1+ progenitors, which expressed the transcription factors *GATA4*, *GATA6*, and *PDX1*, but not *NKX6-1*, indicating that these cells are not yet fully committed towards pancreatic and beta cell differentiation (Xuan and Sussel, 2016); pancreatic progenitor cells (hereafter referred to as NKX6-1+ progenitors), which expressed both *PDX1* and *NKX6-1* and corresponded to the predominant cluster in scRNA-seq; endocrine cells which expressed both endocrine markers *PAX6* and *CHGA* and the pancreatic hormones *INS*, *GCG*, and *SST*; and non-endocrine cells, which we identified as precursors for ductal cells (referred to as early ductal), expressed endothelial marker *FLT1* (Pictet et al., 1972; Reichert and Rustgi, 2011). Similar to Veres et al., we identified a subcluster within the NKX6-1+ progenitors that expressed cell division markers (*TOP2A*, *CENPF*, *AURKB*), indicating that the cells in this cluster were replicating NKX6-1+ progenitors. We also identified primitive cells in the iPSC-PPCs not represented in the Veres et al. study including mesendoderm and early definitive endoderm, which expressed markers for early embryonic development (*COL1A1*, *COL1A2*, *AFP*, and *APOA2*) (Nowotschin et al., 2019; Saykali et al., 2019; Teo et al., 2015) and iPSCs, which expressed the stem cell marker *POUF51* and corresponded to the iPSC scRNA-seq sample. These results are consistent with the differentiation protocol used in Veres et al. (Veres et al., 2019), generating similar albeit more advanced cell types than the differentiation protocol we used to generate the iPSC-PPCs.

While the nine iPSC-PPC samples all consisted of multiple cell types, the vast majority of the scRNA-seq cells were PDX1+ progenitors, NKX6-1+ progenitors or replicating NKX6-1+ progenitors. To determine if our results reflected the differentiation efficiency measured by flow cytometry, we compared the fraction of NKX6-1+ progenitors and replicating NKX6-1+ progenitors, with the fraction of cells that stained double-positive for *PDX1* and *NKX6-1*. We found that these two independent measurements were highly correlated ( $R = 0.843$ ,  $p = 0.00218$ ;

Pearson's correlation, **Figure S7A**), indicating that scRNA-seq captured the variable differentiation efficiency observed in FACS.

To annotate the snATAC-seq clusters, we compared motif activity scores of pancreatic-associated transcription factors from chromVAR (Schep et al., 2017) with their gene expression levels from scRNA-seq (**Figure 1G**, **Table S4**). While most cell types could be identified in both scRNA-seq and snATAC-seq, we observed several differences (**Figure 1**, **Figure S5**, **Figure S6**, **Table S5**, **Table S6**). Both technologies identified mesendoderm (strong motif activity scores for TFAP2A, TFAP2B, (Raap et al., 2021; Wang et al., 2011)), NKX6-1+ progenitors (GATA4/6, HNF4A, FOXA1/2 PDX1, NKX6-1), endocrine (HNF1A, MAFA, NEUROD1, NKX2-2), and early ductal (ETV1, ETS1, ETS2) cell type populations. However, with scRNA-seq, we were able to distinguish clusters of early definitive endoderm cells and *PDX1*+ progenitors, which could not be distinguished in snATAC-seq from *NKX6-1*+ progenitors, which were the predominant cell type. Furthermore, snATAC-seq could not discriminate between replicating and non-replicating iPSC-PPC. However, when we compared the cell type fractions of NKX6-1+ progenitors in snATAC-seq with the fraction of early definitive endoderm, PDX1+, NKX6-1+ progenitors, and replicating cells in scRNA-seq, the fractions were significantly correlated ( $R = 0.956$ ,  $p = 0.000783$ , **Figure S7B**). Interestingly, we identified two distinct endocrine cell clusters using snATAC-seq, which differed in motif activity levels of early endocrine (SOX4, SOX10 and SOX13 (Lioubinski et al., 2003; Xu et al., 2015)) and late endocrine transcription factors (NKX2-2 and NEUROD1 (Doyle and Sussel, 2007; Itkin-Ansari et al., 2005; Mastracci et al., 2013)). Because the early endocrine cells also showed high motif activity levels for PAX and RFX (**Figure 1G**), which regulate endocrine differentiation, we determined that these cells are committed to endocrine lineage but have not yet fully developed into mature endocrine cells. Overall, while our results show that while scRNA-seq and snATAC-seq capture slightly different iPSC-PPC cell types, the predominant cell type across all samples in both assays consisted of NKX6-1+ progenitors.

## **Endocrine cells express combinations of three pancreatic endocrine hormones**



155 ESC-PPCs have been shown to produce polyhormonal endocrine cells (Shahjalal et al., 2018). We tested whether  
156 the 952 cells in the endocrine cluster expressed combinations of *INS* (insulin), *GCG* (glucagon), and *SST*  
157 (somatostatin, **Figure S8**). We observed that 50.7% of endocrine cells expressed *INS*, 18.7% expressed *GCG*, and  
158 30.9% expressed *SST*. Of these cells, 23.7% expressed only one of the three hormones and 32.8% expressed at  
159 least two hormones, with *INS* and *SST* being the most common combination (16%) and 11% expressed all three  
160 hormones. While these hormones were also expressed in non-endocrine cell clusters, they were expressed in less  
161 than 5% of the cells. These results suggest that, while the protocol results in asynchronous differentiation, NKX6-  
162 1+ progenitors, which are the most common cell type in the iPSC-PPCs, represent early pancreatic lineage to  
163 endocrine cells.

### 164 **Characterizing regulatory genetic variation in snATAC-seq**

165 To understand the potential of iPSC-PPC as a model system to study pancreas regulatory genetics, we  
166 investigated the potential effects of variants overlapping 203,895 autosomal snATAC-seq peaks using three  
167 methods: 1) by identifying active transcription footprints and detecting their overlapping variants, using TOBIAS  
168 (Bentsen et al., 2020); 2) by predicting the allelic effects of variants in snATAC-seq peaks, using deltaSVM  
169 (Ghandi et al., 2014; Ghandi et al., 2016; Yan et al., 2021); and 3) by measuring allelic-specific effects (ASE) on  
170 heterozygous variants in snATAC-seq peaks.

171 To annotate accessible chromatin regions in iPSC-PPC, we identified 3,871,477 unique footprints for 746  
172 transcription factors at 57,797 snATAC-seq peaks (28.3%) using TOBIAS (Bentsen et al., 2020; Stormo, 2013).  
173 We observed multiple footprints at the same peak for two reasons: 1) multiple transcription factors may bind to  
174 the same peak; and 2) since TOBIAS identifies transcription factor footprints independently for each transcription  
175 factor and determines the presence of a bound footprint based on each transcription factor motif, it cannot  
176 distinguish between transcription factors with highly similar motifs (for example: NKX6-1 and NKX6-2);

177 therefore, multiple transcription factors in the same family may be identified as bound to the same footprint. To  
178 identify variants with potential effects on transcription factor binding in iPSC-PPC, we selected 325,942 common  
179 SNPs ( $\geq 5\%$  minor allele frequency across 273 iPSCORE individuals (Panopoulos et al., 2017)) in 134,065  
180 snATAC-seq peaks (65.8% of all peaks) and found that 35,248 (10.8%) overlapped at least one of the 3,871,477  
181 active transcription factor footprints, corresponding to 19,775 peaks (9.7%) and 107,354 footprints (Table S7).  
182 Although TOBIAS identifies transcription factor footprints, indicating the genomic loci where a transcription  
183 factor is bound, it does not provide any information or prediction about the potential effects of the genotype of  
184 variants on transcription factor binding.

185 Next, to examine the allelic effects of variants in the snATAC-seq peaks we used recently published HT-SELEX  
186 data (Yan et al., 2021) generated for 94 transcription factors on  $\sim 100,000$  SNPs at T2D loci to train the deltaSVM  
187 model (Ghandi et al., 2014; Ghandi et al., 2016; Yan et al., 2021). This allowed us to use deltaSVM to predict the  
188 allelic effects of the 325,942 common SNPs on the binding of the 94 transcription factors in the 134,065 snATAC-  
189 seq peaks. We found that 52,653 SNPs (16.2%) in 42,511 peaks (20.8%) were predicted to overlap transcription  
190 factor binding sites and to have allelic effects on their binding (Table S7, Table S8). To validate these predictions,  
191 we investigated their overlap with the transcription factor footprints determined using TOBIAS for 89  
192 transcription factors tested with both methods. For each of these transcription factors, we confirmed that variants  
193 predicted by deltaSVM to overlap bound transcription factor binding sites were more likely than expected to  
194 overlap the transcription factor footprint identified by TOBIAS ( $p = 2.2 \times 10^{-47}$ , t-test, Figure S9A, Table S9) and  
195 found a negative association between deltaSVM score and distance from each transcription factor footprint ( $p =$   
196  $4.3 \times 10^{-15}$ , t-test, Figure S9B).

197 Finally, to measure allelic-specific effects in 48,738 snATAC-seq peaks that overlapped at least one SNP  
198 heterozygous in one or more of the seven tested samples (110,290 SNPs in total, including 86,660 of the ones  
199 tested with TOBIAS and deltaSVM, Table S7, Table S10), we utilized genotypes of the nine iPSCORE

individuals from whole genome sequencing (DeBoever et al., 2017; Panopoulos et al., 2017). We divided SNPs according to whether they were heterozygous in one sample (termed “singletons” hereafter: 60,742 SNPs) or two or more samples (“multiplets”: 49,548 SNPs, [Figure S10](#)). We found 3,862 singleton and 3,487 multiplet SNPs with ASE (7,349 in total,  $FDR < 0.05$ , binomial test, adjusted using Benjamini-Hochberg’s method) in 5,583 peaks (2.25% of all peaks). We compared the allelic effects measured by ASE with the estimations by deltaSVM and observed a significantly positive correlation ( $R = 0.26$ ,  $p\text{-value} = 3.0 \times 10^{-34}$ , [Figure 2A](#)). We also computed the correlation between snATAC-seq ASE and the deltaSVM predictions of allelic effects in each of these transcription factors. We observed a significantly positive correlation for 27 transcription factors ( $FDR \leq 0.05$ , Benjamini-Hochberg’s method, [Figure 2B](#), [Table S11](#)) and the distribution of correlation values across all transcription factors was significantly greater than zero ( $p = 3.7 \times 10^{-6}$ , t-test). The transcription factors with the strongest correlation included genes with known functions in embryonic development and pancreas, such as *JDP2* (Huang et al., 2011), *NFE2* (Kojayan et al., 2019), *ATF3* (Fazio et al., 2017), *CUX1* (Ripka et al., 2010) and *FOXBI* (Ma et al., 2016). We also observed a negative association between ASE measured on heterozygous variants in snATAC-seq peaks and their distance from transcription factor footprints ( $p = 6.45 \times 10^{-84}$ , t-test, [Figure S9C](#), [Table S12](#)), indicating that variants with allelic effects are more likely than expected to affect transcription factor binding and that the results from the methods we employed to analyze the associations between genetic variation and chromatin function are concordant. Using three methods (TOBIAS, deltaSVM and ASE), we were able to detect or predict allelic effects or effects on transcription factor binding for 86,261 variants ([Figure 2C](#)). These results indicate that the genotypes of a large proportion of variants at iPSC-PPC snATAC-seq peaks are likely associated with altered binding affinities for transcription factors and therefore may be associated with adult pancreatic complex traits and disorders.

To examine the correlation between ASE in iPSC-PPC regulatory elements due to genetic variation and to changes in gene expression, we performed bulk RNA-seq (scRNA-seq only has coverage at 3’ end of gene) for the seven

223 samples with snATAC-seq and performed ASE on the transcriptome (Figure S10, Table S13). We observed a  
224 significant positive correlation between ASE at promoters and allelic bias with corresponding genes ( $R = 0.039$ ,  
225  $p = 1.6 \times 10^{-6}$ , Figure 2D). Although significant, the correlation between ASE at promoters and corresponding  
226 genes was weak, which is consistent with previous observations (Gate et al., 2018), and could reflect the fact that  
227 multiple proximal and distal regulatory elements can regulate the expression of a gene. Overall, these results show  
228 that regulatory genetic effects are consistent between the epigenome and the transcriptome.

## 229 **Regulatory variants with allelic effects in iPSC-PPC are associated with Type 2 Diabetes**

230 To test if regulatory variants active in iPSC-PPC were associated with Type 2 Diabetes (T2D), we intersected the  
231 iPSC-PPC snATAC-seq peaks with the 380 99% functional credible sets (comprised of 66,607 SNPs) identified  
232 in a meta-analysis of 32 T2D GWAS from about 900,000 individuals (Mahajan et al., 2018). We found that the  
233 majority of credible sets (269, 70.8%) had at least one SNP (3,705 SNPs in total) that overlapped with iPSC-PPC  
234 snATAC-seq peaks (Table S14). These overlapping variants were more likely to have a higher rank (based on  
235 causality within a credible set,  $8.6 \times 10^{-136}$ , Mann-Whitney U test) and a higher posterior probability of association  
236 (PPA) with T2D ( $p = 3.6 \times 10^{-68}$ ) than SNPs outside of peaks (Figure 3A,B). These results indicate that regulatory  
237 elements active in iPSC-PPC are enriched for causal variants associated with T2D.

238 To further characterize the potential of iPSC-PPC to study T2D genetics, we identified variants in the T2D  
239 credible sets that had high PPA or were the top-ranked and overlapped bound transcription factor binding sites  
240 (TOBIAS), had predicted allelic effects (deltaSVM) and/or validated allelic effects (ASE). Of the 269 credible  
241 sets with at least one SNP overlapping snATAC-seq peaks, 209 (77.7%) had at least one SNP potentially altering  
242 transcription factor binding affinities, including 163 with TOBIAS support, 152 with deltaSVM support and 65  
243 with ASE. Of note, 73 had support from two methods and six from all three (Table S14). Among these 209 T2D

244 loci, we found 65 SNPs that showed strong evidence of being causal, including 38 that were top-ranked and 27  
245 that were not the top ranked but had high PPA (PPA > 10%, **Figure 3C**).

246 The 38 SNPs that were the top-ranked included six with PPA  $\geq$  90%, corresponding to the loci for *GLI2* (predicted  
247 to affect binding by deltaSVM and/or TOBIAS of HSF2, HSF4 and YY2), *CHCR2* (RFX1-5, SCRT1, SCRT2),  
248 *UBAP2* (HSF2 and HSF4), *SLC30A8* (PAX1 and PAX9), *IGF2BP2* (IRF1, PRDM1, ZNF384, and shows ASE  
249 in snATAC-seq) and *DGKB* (RFX1) and eight with PPA between 50% and 90%, corresponding to *KCNQ1*  
250 (ZNF148 and ZNF263, and shows ASE in snATAC-seq), *PTPN9* (HNF4A, HNF4G, NR4A1 and XBP1), *PPARG*  
251 (*PPARG*, *RXRA* and *PROX1*), *MTNR1B* (HSF2), *MAP2K7* (ZNF423), *RREB1* (ZBTB33), *HHEX/IDE* (ZNF460)  
252 and *LCORL* (*ASCL1*, *ASCL2*, *BHLHE22*, *MYF5*, *MYOD1*, *MYOG*, *NHLH1*, *PTF1A*, *TCF12*, *ZBTB18* and  
253 *ZSCAN29*, **Table S14**). Many of the 209 potentially altered binding sites were associated with transcription  
254 factors with pancreatic functions: *HSF4* is expressed in pancreas and is associated with neuronal development  
255 (Nakai et al., 1997; Syafruddin et al., 2021); and YY2 is involved in the regulation of multiple cellular processes,  
256 including pluripotency and differentiation (Li et al., 2020); RFX3 is involved in pancreatic endocrine cells  
257 development (Ait-Lounis et al., 2007); SCRT1 is involved in the regulation of beta cell proliferation during  
258 differentiation (Sobel et al., 2021); IRF1 regulates the progression of pancreatic cancer (Sakai et al., 2014);  
259 ZNF148 is associated with pancreatic cancer risk (Fang et al., 2017); variants in HNF4A causes maturity-onset  
260 diabetes of the young and are associated with T2D (Yamagata, 2014); HNF4G is associated with glucose tolerance  
261 (Baraille et al., 2015); NR4A1 protects beta cells from apoptosis (Yu et al., 2015); XBP1 is required for the  
262 homeostasis of acinar cells (Hess et al., 2011); PPARG regulates multiple insulin-associated genes in beta cells  
263 (Gupta et al., 2010); RXRA negatively regulates glucose-stimulated insulin secretion (Miyazaki et al., 2010);  
264 PROX1 controls pancreas morphogenesis (Wang et al., 2005); PTF1A regulates acinar cell apoptosis (Sakikubo  
265 et al., 2018).

266 Twenty-seven credible sets had SNPs with allelic effects that were not the top ranked but had high PPA (PPA >  
267 10%). These cases include the *ZNF169* locus, whose top-ranked SNP (rs12236906) has PPA = 33% but does not  
268 overlap any snATAC-seq peak, whereas its second-ranked SNP (rs10993329, PPA = 31%) overlaps a snATAC-  
269 seq peak and has deltaSVM predicted allelic effects (**Figure 3D**). Although rs12236906 has been indicated as the  
270 most likely causal SNP for this locus, our results suggest that rs10993329 is more likely to be functional. These  
271 observations are supported by the higher activity of the genomic region surrounding rs10993329 across multiple  
272 tissues (**Figure 3D**). We further investigated the predicted allelic effects of rs10993329 and found that it is  
273 associated with the loss of motifs for three members of the ETS family of transcription factors (ERG, FEV and  
274 FLI1), which play a role in pancreatic mesodermal development (Kobberup et al., 2007).

275 In the *KSR2* locus, the variants with the second- and third-highest PPA (rs79310463: 25%; and rs34965774: 13%)  
276 have both been described as causal for T2D and are both included in the GWAS Catalog (Buniello et al., 2019),  
277 whereas the variant with the highest PPA (rs55834317: 27%) is not associated with any GWAS. While  
278 rs79310463 and rs55834317 both overlap a snATAC-seq peak, only rs79310463 is associated with ASE and  
279 overlaps footprints for TFDP1 and ZNF263, suggesting that this SNP is more likely to have functional  
280 consequences in this locus (**Figure 3E**).

281 In other loci containing lower ranked SNPs (PPA > 10%), such as *HMG20A* and *IRS2*, multiple variants overlap  
282 iPSC-PPC snATAC-seq peaks and are predicted to have ASE, indicating that additional studies are needed to  
283 determine if multiple causal SNPs underlie the associations in these loci and whether they are functional. In  
284 conclusion, our genetic association analysis shows that many regulatory variants implicated in T2D are active  
285 and have allelic effects in iPSC-PPC, making these cells a suitable model system to identify and characterize the  
286 molecular mechanisms underlying T2D genetic associations.

## 287 Discussion

288 In this study, we derived ten iPSC-PPC samples from nine unrelated individuals to generate matched scRNA-seq  
289 and snATAC-seq and determined that while the differentiation was asynchronous and similar to ESC-PPC (Veres  
290 et al., 2019), the derived cells largely consisted of a single cell type (NKX6-1+ progenitors). We characterized  
291 regulatory variants that overlapped open chromatin in iPSC-PPC and found that these variants are likely to have  
292 allelic effects on chromatin accessibility and may affect transcription factor binding. To validate the utility of  
293 iPSC-PPC to characterize and annotate genetic variants associated with adult T2D, we used previously fine-  
294 mapped 380 T2D risk loci (Mahajan et al., 2018). Enrichment analyses revealed that the majority of the T2D risk  
295 loci were located within open chromatin regions of iPSC-PPC. Furthermore, these loci contain variants that  
296 overlap active transcription factor binding sites and/or show allele specific effects on chromatin accessibility.

297 Our study identified 65 T2D risk loci containing SNPs with strong evidence of being causal (i.e. high PPA) that  
298 are associated with allelic-specific effects and/or predicted to affect transcription factor binding in the iPSC-PPCs.  
299 For 38 of the T2D risk loci, the top-ranked SNP (i.e. the SNP with highest PPA) had functional effects on  
300 transcription factor binding and/or chromatin accessibility; while in 27 loci, we observed that at least one lower-  
301 ranked SNP with high PPA ( $\geq 10\%$ ) was associated with allelic effects or altered transcription factor binding,  
302 suggesting that the top-ranked SNP is likely not causal. In certain cases, such as rs79310463 in the *KSR2* locus,  
303 the SNP we identified as being associated with allelic effects or transcription factor binding had been described  
304 as being causal in previous T2D studies (Ishigaki et al., 2020; Suzuki et al., 2019; Vujkovic et al., 2020); whereas  
305 in other loci (rs10993329 in the *ZNF169* locus), the SNP we predict to have functional effects had not previously  
306 been associated with T2D. Fine mapping using regulatory annotations, such as chromatin state maps in relevant  
307 tissues (Ernst and Kellis, 2012; Roadmap Epigenomics et al., 2015), prioritizes SNPs that overlap specific  
308 annotations (Pickrell, 2014); however, it is challenging to distinguish causal SNPs from variants that are in high  
309 LD with it. Here, we showed that characterizing the functional effects of individual SNPs using TOBIAS (Bentsen

310 et al., 2020), deltaSVM predictions (Ghandi et al., 2014; Ghandi et al., 2016; Yan et al., 2021) or ASE, provides  
311 an alternative method to pinpoint the likely causal SNPs and may help discriminate neutral SNPs that are in high  
312 LD. Although the analyses proposed here identified SNPs that are associated with the active regulatory elements  
313 in iPSC-PPC, further analyses that integrate the results presented here with co-accessibility, expression  
314 quantitative trait loci (eQTLs) (Vinuela et al., 2020), chromatin accessibility QTLs (Alasoo et al., 2018),  
315 colocalization between QTLs and GWAS (Giambartolomei et al., 2014; Giambartolomei et al., 2018; Majumdar  
316 et al., 2018; Wallace, 2020) and, ultimately, experimental validation (Geusz et al., 2020), are needed to link their  
317 effects with their target genes and thus, functional mechanisms, as most regulatory elements are not in close  
318 proximity to promoters, and distal regulatory elements may regulate multiple genes (Oh et al., 2021). By  
319 empowering chromatin accessibility profiles with advanced tools such as transcription factor footprinting, allelic  
320 effect predictions, and co-accessibility, it is feasible to uncover novel molecular mechanisms that underlie the  
321 genetic risk of T2D.

322 Our study shows that by combining GWAS with epigenomic information from iPSC-PPC, it is feasible to gain  
323 insight into the molecular mechanisms underlying the associations between genetic variation and adult pancreatic  
324 complex traits and disease. Although we were able to determine the associations between SNPs in 209 T2D risk  
325 loci and transcription factor binding or allelic effects, the majority of the associations were predictions. Larger  
326 sample sizes would result in additional variants in ATAC-seq peaks and greater statistical power to test each  
327 variant-containing peak for ASE and downstream changes in gene expression. Indeed, to gain insight into global  
328 functional genetic variation, it will be necessary to obtain data for hundreds of iPSC-PPCs. With a small sample  
329 size, we show that iPSC-PPC provide a suitable model system to study the associations between genetic variation,  
330 regulatory mechanisms, and T2D, and that studies involving large numbers of samples could aid in the  
331 identification of causal variants at the majority of T2D risk loci.



## 332 **Methods**

### 333 **iPSCORE subject information**

334 We obtained 9 iPSC lines from the iPSCORE collection (Panopoulos et al., 2017) (**Table S1**). These lines were  
335 reprogrammed from skin fibroblasts collected from 9 unrelated subjects (8 female, 1 male), who ranged in age at  
336 time of donation from 21 to 65 years old, and represent three 1000 Genomes Project super populations: European  
337 American (7), Asian American (1), and African American (1). From each subject, whole blood samples were  
338 collected and used to generate and process whole genome sequence (WGS) data as previously described  
339 (D'Antonio et al., 2018; DeBoever et al., 2017). Briefly, reads were aligned against human genome b37 with  
340 decoy sequences (Genomes Project et al., 2015) using BWA-mem and default parameters (Li and Durbin, 2009).  
341 We applied the GATK best-practices pipeline for variant calling that includes indel-realignment, base-  
342 recalibration, genotyping using HaplotypeCaller, and finally joint genotyping using GenotypeGVCFs (DePristo  
343 et al., 2011; McKenna et al., 2010; Van der Auwera et al., 2013). The recruitment of these individuals was  
344 approved by the Institutional Review Boards of the University of California, San Diego and The Salk Institute  
345 (Project no. 110776ZF).

### 346 **iPSC-PPC Derivation**

347 iPSC-PPCs were derived using STEMdiff™ Pancreatic Progenitor Kit (StemCell Technologies) following  
348 manufacture's recommendations except as noted below. One iPSC line (from subject 90e8222f-2a97-4a3c-9517-  
349 fbd7626122fd) was independently differentiated twice (PPC\_029 and PPC\_036) resulting in a total of 10 derived  
350 iPSC-PPC samples.

351 *Expansion of iPSC:* One vial from each of 9 iPSC lines was thawed into mTeSR1 medium containing 10  $\mu$ M  
352 ROCK Inhibitor (Selleckchem) and plated on one well of a 6-well plate coated with matrigel. iPSCs were grown

353 until they reached 80% confluency and then passaged using 2mg/ml solution of Dispase II (ThermoFisher  
354 Scientific). To obtain a sufficient number of iPSCs for differentiation, iPSCs were passaged twice: 1) cells from  
355 the first passage were plated on three wells of a 6-well plate (ratio 1:3); and 2) cells from the second passage were  
356 plated on six wells of a 6-well plate (ratio 1:2).

357 *Monolayer plating (Day 0; D0)*: When the confluency of iPSC cells in the six wells of a 6-well plate reached  
358 80%, cells were dissociated into single cells using Accutase (Innovative Cell Technologies Inc.). Single iPSC  
359 cells were resuspended at the concentration of  $1.85 \times 10^6$  cells/ml in mTeSR containing  $10 \mu\text{M}$  ROCK inhibitor  
360 and plated on six wells of a 6-well. Cells were grown for approximately 16 to 20 hours to achieve a uniform 90-  
361 95% confluency ( $3.7 \times 10^6$  cells/well; about  $3.9 \times 10^5$  cells/cm<sup>2</sup>).

362 *Differentiation*: Differentiation of the confluent iPSC monolayers were initiated by the addition of STEMDiff  
363 Stage Endoderm Basal medium supplemented with Supplement MR and Supplement CJ (2ml/well) (D1). All  
364 following media changes were performed every 24 hours following initiation of differentiation (2ml/well). On  
365 D2 and D3, the medium was changed to fresh STEMDiff Stage Endoderm Basal medium supplemented with  
366 Supplement CJ. On D4, the medium was changed to STEMDiff Pancreatic Stage 2-4 Basal medium supplemented  
367 with Supplement 2A and Supplement 2B. On D5 and D6, the medium was changed to STEMDiff Pancreatic  
368 Stage 2-4 Basal medium supplemented with Supplement 2B. On D7, D8 and D9, the medium was changed to  
369 STEMDiff Pancreatic Stage 2-4 Basal medium supplemented with Supplement 3. On D10, D11, D12, D13 and  
370 D14, the medium was changed to STEMDiff Pancreatic Stage 2-4 Basal medium supplemented with Supplement  
371 4.

372 *Harvest*: On D15 cells were dissociated using Accutase, collected and counted, and either processed fresh  
373 (scRNA-seq) or cryopreserved (scRNA-seq and snATAC-seq).

## 374 **Flow Cytometry**

375 Each of the 10 iPSC-PPC differentiations were analyzed for co-expression of two pancreatic precursor markers,  
376 PDX1 and NKX6-1, using flow cytometry. Specifically, at least  $2 \times 10^6$  iPSC-PPC cells were fixed and  
377 permeabilized using the Fixation/Permeabilization Solution Kit with BD GolgiStop™ (BD Biosciences)  
378 following manufacturer recommendations. After the last centrifugation, cells were resuspended in 1X BD  
379 Perm/Wash™ Buffer at the concentration of  $1 \times 10^7$ /ml. For each flow cytometry staining,  $2.5 \times 10^5$  cells were  
380 stained with PE Mouse anti-PDX1 Clone-658A5 (BD Biosciences; 1:10) and Alexa Fluor® 647 Mouse anti-  
381 NKX6.1 Clone R11-560 (BD Bioscience; 1:10) or with appropriate class control antibodies, PE Mouse anti-IgG1  
382  $\kappa$  R-PE Clone MOPC-21 (BD Biosciences) and Alexa Fluor® 647 Mouse anti IgG1  $\kappa$  Isotype Clone MOPC-21  
383 (BD Biosciences). Cells were stained for 75 minutes at room temperature, washed three times, resuspended in  
384 PBS containing 1% BSA and 1% Formaldehyde, and immediately processed through FACS Canto II flow  
385 cytometer. FACS results were analyzed using FlowJo software V 10.4. The fractions of PDX1 and NKX6-1-  
386 positive cells varied across the analyzed iPSC-PPC lines, where percentages of PDX1/NKX6-1 double-positive  
387 cells ranged from 14.6 – 91.7% (mean = 60.0%; median = 71.0%).

## 388 **Generation of scRNA-seq**

389 *Library Generation:* One 1 iPSC line (from subject: iPSC\_PPC034) and 10 iPSC-PPC samples were used for  
390 scRNA-seq generation ([Table S1](#)). Fresh cells (i.e., not frozen) from the iPSC line and from seven iPSC-PPC  
391 samples were captured individually at D15. Four of these same iPSC-PPC samples were also captured as  
392 cryopreserved cells (immediately after thawing) along with three iPSC-PPC samples that were captured only as  
393 cryopreserved cells. Cells from four cryopreserved iPSC-PPC samples were pooled (RNA\_Pool\_1), and cells  
394 from the other 3 iPSC-PPC samples were pooled (RNA\_Pool\_2) prior to capture ([Table S1](#)). All single cells were  
395 captured using the 10x Chromium controller (10x Genomics) according to the manufacturer's specifications and  
396 manual (Manual CG000183, Rev A). Cells from each scRNA-seq sample (1 iPSC, 7 fresh iPSC-PPCs,  
397 RNA\_Pool\_1, and RNA\_Pool\_2) were loaded on an individual lane of a Chromium Single Cell Chip B. Libraries

were generated using Chromium Single Cell 3' Library Gel Bead Kit v3 (10x Genomics) following manufacturer's manual with small modifications. Specifically, the purified cDNA was eluted in 24µl of Buffer EB, half of which was used for the subsequent step of the library construction. cDNA was amplified for 10 cycles and libraries were amplified for 8 cycles.

*Sequencing:* Libraries produced from fresh and cryopreserved cells were sequenced on a HiSeq 4000 using custom programs (fresh: 28-8-175 Pair End and cryopreserved: 28-8-98 Pair End). Specifically, 8 libraries generated from fresh samples (1 iPSC and 7 iPSC-PPC samples) were pooled together and loaded evenly on 8 lanes and sequenced to an average depth of 163 million reads. Two libraries from seven cryopreserved lines (RNA\_Pool\_1 and RNA\_Pool\_2) were each sequenced on an individual lane to an average depth of 265 million reads. In total, we captured 99,819 cells. **Figure S2** shows highly similar cell type proportions are observed in fresh and cryopreserved iPSC-PPCs.

## Processing scRNA-seq data

*Raw data processing.* We retrieved FASTQ files for 10 scRNA-seq samples (one iPSC, seven fresh iPSC-PPCs, one RNA\_Pool\_1, and one RNA\_Pool\_2) and used CellRanger V6.0.1 (<https://support.10xgenomics.com/>) with default parameters and v34lift37 (Harrow et al., 2012) gene annotations to generate single-cell gene counts and BAM files for each individual sample (**Table S1**).

*Demultiplexing.* To reassign pooled cells iPSC-PPCs back to the original subject (RNA\_Pool\_1 and RNA\_Pool\_2; **Table S1**), we obtained the BAM files for each scRNA-seq sample and a VCF file containing SNPs (called from WGS) that are bi-allelic and located at UTR or exon regions on autosomes as annotated by Gencode v34lift37 (Harrow et al., 2012) calls from each of the nine subjects, two of which was not included in scRNA-seq pools but served as negative controls. The two files (BAM and VCF) were used as input to Demuxlet (Kang et al., 2018), which outputted the subject identities of each single cell based on genotype. We found that less than

420 1% of the cells mapped to negative controls after filtering for low quality cells and thus, were removed from  
421 downstream analyses.

422 *Data Processing.* To merge the 10 scRNA-seq samples (1 iPSC, 7 fresh iPSC-PPCs, RNA\_Pool\_1, and  
423 RNA\_Pool\_2), we first aggregated the samples that were sequenced as an independent batch (1 iPSC and 7 fresh  
424 iPSC-PPC) using the CellRanger V6.0.1 command *aggr* with no normalization. For each sample (aggregated  
425 sample, RNA\_Pool\_1, and RNA\_Pool\_2), we log-normalized the gene counts (*NormalizeData*) and identified  
426 the 2000 most variables genes using a threshold of 0.5 for the standardized log dispersion (*FindVariableFeatures*).  
427 We next applied Seurat's standard integration workflow to adjust for batch differences between the samples.  
428 Specifically, we used *FindIntegrationAnchors* to identify a set of integration anchors between the samples using  
429 30 dimensions computed from canonical correlation analysis (CCA). Next, we integrated the samples using  
430 *IntegrateData* and applied the standard downstream workflow of scaling the data (*ScaleData*), applying principle  
431 dimension reduction for 30 principle components (*RunPCA*), and then visualizing the single cells using Uniform  
432 Manifold Approximation and Projection (UMAP). To identify clusters, we used a shared-nearest-neighbor (SNN)  
433 graph of the significant PCs. To remove poor quality cells, we removed cells with fewer than 500 genes/cell or  
434 more than 50% of the reads mapping to the mitochondrial chromosome. We performed iterative clustering until  
435 all clusters driven by high mitochondrial reads or low number of genes were removed. Clusters with fewer than  
436 250 cells were also removed. After filtering, 83,971 cells remained. We tested resolutions 0.05, 0.08, and 0.1 for  
437 clustering analyses and determined that 0.08 was more representative of the cell types predicted to be observed  
438 during stem cell differentiation into PPCs (Figure 1B,F, Figure S3).

### 439 **Annotation and validation of iPSC-PPC cells in scRNA-seq**

440 To annotate the 83,971 iPSC-PPC cells, we used the expression of markers with known associations with  
441 pancreatic development and function, including *COL1A1*, *COL1A2* (mesendoderm) *AFP*, *APOA* (early definitive

442 endoderm), *GATA4*, *GATA6*, *PDX1* (*PDX1+* progenitors), *PDX1*, *NKX6-1* (*NKX6-1+* progenitors), *PAX6*,  
443 *CHGA*, *INS*, *GCG*, *SST* (endocrine), *FLT1* (early ductal). We used *POU5F1* to identify the iPSC cluster. To obtain  
444 z-normalized expression values, we used cells with normalized expression values above 1% of the maximal  
445 expression, computed the average for each cluster, and then z-normalized across the 8 clusters. To validate cell  
446 type assignments, we used a reference scRNA-seq dataset from the ESC-B time course that captured cells from  
447 four differentiation stages (Veres et al., 2019): Stage 3 (Day 6; 7,982 cells), Stage 4 (Day 13; 6,960 cells), Stage  
448 5 (Day 18; 4,193 cells), and Stage 6 (Day 25; 5,186 cells). Processed single cell gene counts and their associated  
449 metadata were downloaded from GEO (GSE114412). Z-normalized expression values were computed using the  
450 same procedure. We examined the transcriptome profiles at resolutions 0.05, 0.08, and 0.1, and found that the  
451 subclusters within the predominant cluster exhibited similar profiles to each other (Figure 1F, Figure S3, Table  
452 S2), confirming that they were *NKX6-1+* progenitors. To identify differentially expressed genes, we performed  
453 Wilcoxon rank sum test between the normalized expression values of cells within the cluster and cells outside of  
454 the cluster (Table S3). P-values were adjusted using a Bonferroni correction, and genes with  $FDR \leq 0.05$  were  
455 considered differentially expressed.

## 456 **Generation of snATAC-seq**

457 *Library Generation:* A total of 7 iPSC-PPC samples were used for snATAC-seq generation (Table S1). Cells  
458 from seven cryopreserved iPSC-PPCs samples were captured for snATAC-seq immediately after thawing. All  
459 seven samples have matched scRNA-seq. Cells from four cryopreserved iPSC-PPC samples were pooled  
460 (ATAC\_Pool\_1) and cells from the other 3 iPSC-PPC samples were pooled (ATAC\_Pool\_2) prior to capture  
461 (Table S1). Nuclei from two pools were isolated according to the manufacturer's recommendations (Manual  
462 CG000169, Rev B), transposed, and captured as independent samples according to the manufacturer's  
463 recommendations (Manual CG000168, Rev B). All single nuclei were captured using the  
464 10x Chromium controller (10x Genomics) according to the manufacturer's specifications and manual (Manual  
22

465 CG000168, Rev B). Cells for each sample were loaded on the individual lane of a Chromium Chip E. Libraries  
466 were generated using Chromium Single Cell ATAC Library Gel & Bead Kit (10x Genomics) following  
467 manufacturer's manual (Manual CG000168, Rev B). Sample Index PCR material was amplified for 11 cycles.  
468 *Sequencing*: Libraries were sequenced using a custom program (50-8-16-50 Pair End) on HiSeq 4000.  
469 Specifically, two libraries from seven cryopreserved iPSC-PPC samples (ATAC\_Pool\_1 and ATAC\_Pool\_2)  
470 were each sequenced on an individual lane.

## 471 **Processing snATAC-seq data**

472 *Raw data processing*. For two snATAC-seq samples (ATAC\_Pool\_1 and ATAC\_Pool\_2; **Table S1**), we retrieved  
473 FASTQ files and used CellRanger V2.0.0 (<https://support.10xgenomics.com/>) to align files to the hg19 genome  
474 using *cellranger-atac count* with default parameters. NarrowPeaks were called using the MACS2 command  
475 *macs2 callpeak --keep-dup all --nomodel --call-summits* (Feng et al., 2012) on the BAM files merged from the  
476 two pooled samples and detected 288,813 peaks. Peaks called on ambiguous chromosomes or the mitochondrial  
477 genome were removed, leaving 280,079 peaks remaining. Using these peaks, each snATAC-seq sample was  
478 reanalyzed using *cellranger-atac reanalyze* to generate single-nuclei peak counts for each sample. To integrate  
479 the two snATAC-seq datasets for downstream analyses, we performed Signac integration (Butler et al., 2018) by  
480 first applying normalization (*RunTFIDF*) and linear dimensional reduction (*FindTopFeatures* and *RunSVD*) on  
481 each sample dataset. We then identified a random subset of 20,000 peaks and computed a set of integration  
482 anchors between the samples (*FindIntegrationAnchors* for 2,000 anchors) The two snATAC-seq was integrated  
483 using *IntegrateData* and 2-30 most significant dimensions calculated from dimension reduction analyses. Finally,  
484 on the integrated dataset, dimension reduction was applied (*RunSVD* for 30 singular values), and single cells were  
485 visualized using UMAP (*RunUMAP* on 2:30 dimensions). Clusters were identified using a SNN-graph method  
486 using *FindNeighbors* and *FindClusters*. To remove low quality cells, we removed cells that satisfy one of the

487 following criteria: 1) the number of peak region fragments < 2,000 or > 20,000, 2) the percentage of reads in  
488 peaks < 40%, 3) nucleosome signal > 1.5, or 4) TSS enrichment score < 2.5. Furthermore, we removed cells that  
489 do not visually belong to a cluster (i.e. cells that are scattered between two distinct clusters). We performed  
490 iterative clustering until we do not observe significant outliers of single cells. After filtering, 25,564 nuclei  
491 remained and clustering resolutions of 0.1, 0.15, and 0.2 were tested.

492 *Demultiplexing.* To reassign pooled nuclei back to the original subject from two snATAC-seq samples  
493 (ATAC\_Pool\_1 and ATAC\_Pool\_2; [Table S1](#)), we applied Demuxlet (Kang et al., 2018) to the two samples using  
494 the same set of reference variants as stated above.

### 495 **Annotation of iPSC-PPC nuclei in snATAC-seq using chromVAR**

496 To determine the cell types within the integrated snATAC-seq dataset, we used chromVAR (Schep et al., 2017)  
497 within the Signac pipeline to identify transcription factor motifs from the JASPAR 2020 database (Fornes et al.,  
498 2020) that are enriched for accessible chromatin for each cluster. Specifically, we used the *RunChromVAR*  
499 function in Signac and the hg19 reference (BSgenome.Hsapiens.UCSC.hg19) to compute a deviation z-score for  
500 each motif in each cell. To annotate the cell types, we examined the motif activities of transcription factors with  
501 known developmental or pancreatic functions: TFAP2A/B (mesendoderm), GATA4/6 (PDX1+ progenitors),  
502 HNF4A, FOXA1/2, PDX1, NKX6-1 (NKX6-1+ progenitors), HES1, SOX4/9/10/13 (early endocrine), PAX4/6,  
503 RFX1/3, HNF1A, MAFA, NKX2-2, NEUROD1 (endocrine), and ETV1, ETS1, ETS2 (early ductal). To validate  
504 our annotations, we compared the motif activities to their gene expression in scRNA-seq using the same z-  
505 normalization method. We examined the motif activity profiles at resolutions 0.1, 0.15, and 0.20 ([Figure 1G](#),  
506 [Figure S4](#), [Table S4](#)), and reasoned that because subclusters within the predominant cluster expressed both PDX1  
507 and NKX6-1 but at varying levels, we collapsed these clusters into NKX6-1+ progenitors. Resolution 0.1 was  
508 used for downstream analyses. To identify differentially expressed peaks, we applied the *FindAllMarkers* function



509 in Signac with default parameters. Peaks with  $FDR \leq 0.05$  were considered differentially expressed (Table  
510 S5).

### 511 **chromVAR motif enrichment analyses**

512 To identify differentially enriched motifs for each snATAC-seq cluster at resolutions of 0.1, 0.15, and  
513 0.20, we computed a Wilcoxon rank sum test for each motif and cell type cluster, comparing the  
514 chromVAR z-score distributions of a random sample of 2,000 cells within the cluster and a random  
515 sample of 2,000 cells outside of the cluster. Then, for each cluster, we applied a Bonferroni correction to  
516 account for multiple testing. Motifs with  $FDR \leq 0.05$  were considered differentially enriched (Table S6).

### 517 **Processing transcription factor footprints using TOBIAS**

518 To characterize regulatory variants for transcription factor binding sites, we used TOBIAS (Bentsen et al., 2020)  
519 to identify the binding sites of transcription factors. We merged BAM files from snATAC\_Pool\_1 and  
520 snATAC\_Pool\_2 and corrected for bias from Tn5 cutsites using TOBIAS function *ATACorrect*. Using the cutsite  
521 tracks from *ATACorrect*, we computed footprint scores across the regions using *FootprintScores*. Using the  
522 footprint scores along with transcription factor binding motifs from JASPAR2020 (Fornes et al., 2020), we then  
523 estimated the binding positions of each transcription factor footprint across the genome. Using these positions,  
524 we calculated the distance of each of the 325,942 SNPs in snATAC-seq peaks from its closest transcription factor  
525 footprint on the same peak using *bedtools closest -d*. Information about the footprints can be found in Table S7.

### 526 **Prediction of allelic effects using deltaSVM**

527 We obtained deltaSVM (Ghandi et al., 2014; Ghandi et al., 2016) models on 94 transcription factors from the  
528 Genetic Variants Allelic TF Binding Database (GVATdb) (Yan et al., 2021). As training sets for the deltaSVM

529 models, GVATdb includes the results from a SNP-SELEX experiment that analyzed the allelic effects of 95,886  
530 noncoding variants located in close proximity with 110 T2D loci on transcription factor binding. Although  
531 GVATdb investigated 533 transcription factors, only 94 were associated with high-confidence deltaSVM models  
532 (Yan et al., 2021) and were used in this study. We selected 325,942 SNPs with at least 5% minor allele frequency  
533 in the iPSCORE cohort (Panopoulos et al., 2017) that overlapped the 203,895 snATAC-seq peaks using bcftools  
534 (Danecek et al., 2021). We found that 134,065 peaks had overlapping SNPs. We ran the deltaSVM pipeline  
535 developed within GVATdb (<https://github.com/ren-lab/deltaSVM>) on each of these variants. This resulted in  
536 30,638,548 tests (325,942 SNPs by 94 transcription factors). To detect SNPs with a predicted allelic effect on  
537 transcription factor binding, we filtered these tests based on *seq\_binding* == "Y" and *preferred\_allele* != "None".  
538 *seq\_binding* refers to whether the transcription factor is predicted to be bound to the locus overlapping the tested  
539 SNP and *preferred\_allele* describes whether the SNP is associated with improved binding affinity for the  
540 transcription factor ("Gain"), decreased binding affinity ("Loss") or is not associated with changes in transcription  
541 factor binding affinity ("None"). We found 84,196 tests passing these filters, for a total of 52,653 unique SNPs,  
542 as one SNP may be predicted to affect the binding affinity for more than one transcription factor.

### 543 **Allele-specific effects in snATAC-seq peaks**

544 We filtered the total 288,813 snATAC-seq peaks to include peaks on autosomal chromosomes, with MACS2  
545 score  $\geq 100$ , and outside of ENCODE blacklist regions (hg19-blacklist.v2.bed.gz) (Amemiya et al., 2019;  
546 Consortium, 2012). We intersected the resulting 203,895 peaks with the SNPs heterozygous in at least one of the  
547 seven samples that underwent snATAC-seq (Figure S10). Variant information was obtained from our previously  
548 published whole genome sequencing (dbGaP: phs001325) (DeBoever et al., 2017; Jakubosky et al., 2020a;  
549 Jakubosky et al., 2020b). We obtained 110,290 SNPs with read depth  $\geq 20$  in at least one heterozygous sample,  
550 which we divided into: 1) 60,742 SNPs heterozygous only in one sample (singletons); and 2) 49,548 SNPs  
551 heterozygous in multiple samples (multiplets). We calculated allele-specific effects (ASE) for each SNP

independently in each heterozygous sample using a two-sided binomial test with the alternative hypothesis that both alleles were equally likely to be observed ( $p = 0.5$ ). We further removed all multipliers with inconsistent effects: only 22,717 multiplier SNPs (61,562 tests) having the sign of  $\log_2\left(\frac{reads_{REF}}{reads_{ALT}}\right)$  consistent across all heterozygous samples were retained for downstream analyses. FDR correction was performed on a per-sample basis using Benjamini-Hochberg's method on all singleton and multiplier SNPs passing this filter (17,199 – 36,517 tests).

To test for the correspondence between ASE in snATAC-seq and bulk RNA-seq, we obtained the coordinates of Genecode v34lift37 (Harrow et al., 2012) promoters and intersected them with coordinates of snATAC-seq peaks displaying ASE using *bedtools intersect*. We obtained 826 and 759 genes whose promoters overlapped singleton and multiplier SNPs, respectively. Of these genes, we retained 447 and 497, respectively, that were expressed (TPM > 1 in the heterozygous samples) and that had read depth  $\geq 10$  for at least one heterozygous variant.

## Generation of bulk RNA-seq

*Library generation and sequencing:* For 10 iPSC-PPC samples, RNA was isolated from total-cell lysates using the Quick-RNA<sup>TM</sup> MiniPrep Kit (Zymo Research) with on-column DNase treatments. RNA was eluted in 48ul RNase-free water and analyzed on a TapeStation (Agilent) to determine sample integrity. All iPSC-PPC samples had RNA integrity number (RIN) values between 9.4 and 10. Illumina TruSeq Stranded mRNA libraries were prepared and sequenced on HiSeq 4000 to an average depth of 58.6 M 100-bp paired-end reads per sample.

*Raw data processing.* FASTQ files were obtained for the 10 iPSC-PPC samples and processed with a similar pipeline used in our previous studies (D'Antonio-Chronowska et al., 2019; D'Antonio et al., 2021; DeBoever et al., 2017). Briefly, RNA-seq reads were aligned with STAR (2.7.3) (Dobin et al., 2013) to the hg19 reference using Genecode v34lift37 (Harrow et al., 2012) splice junctions with default alignment parameters and the following adjustments: *-outFilterMultimapNmax 20, -outFilterMismatchNmax 999, -alignIntronMin 20, -*

574 *alignIntronMax 1000000, -alignMatesGapMax 1000000*. Bam files were sorted by coordinates using Samtools  
575 (1.9.0), and duplicate reads were marked using Samtools (1.9.0) (Danecek et al., 2021). TPM values were  
576 estimated from STAR transcriptome bam file using RSEM (1.2.20) (Li and Dewey, 2011). RNA-seq QC metrics  
577 were collected from Samtools (1.9.0) flagstat and idxstats and/or Picard (2.20.1) *CollectRnaSeqMetrics* (2019).  
578 *Sample quality control*. To confirm the subject identify assigned to each bulk RNA-seq, we tested common  
579 variants from the 1000 Genomes Phase 3 panel (Genomes Project et al., 2015) that are bi-allelic and have minor  
580 allele frequency between 45% to 55%. For each sample, genotype likelihoods were estimated using BCFtools  
581 (Danecek et al., 2021) (1.9.0) mpileup relative to the hg19 reference, and genotypes were called using BCFtools  
582 (1.9.0) *call*. Genotypes were filtered by a threshold of 10 for total read depth. Identity-by-state (IBS) was then  
583 estimated with PLINK (Purcell et al., 2007) *genome* for each pairwise comparison between the inferred genotypes  
584 from RNA-seq and the genotypes from WGS. RNA-seq samples were correctly matched with the subjects based  
585 on the highest *pihat* for each RNA-seq and individual pair.

### 586 **Allele-specific effects in bulk RNA-seq using MBASED**

587 To detect the allele-specific effects of gene expression in bulk RNA-seq from seven samples (7 subjects), we used  
588 an R package MBASED (Mayba et al., 2014), which uses a meta-analysis approach that aggregates information  
589 from all SNPs within the gene body to measure gene-level ASE. For ASE analysis, we only considered genes on  
590 autosomes and that is expressed. We determined a gene to be expressed if the gene is expressed with at least 1  
591 TPM in at least 10% of the seven samples. Of the 62,492 genes, 18,217 genes (29.2%) were expressed, of which  
592 10,715 were on autosomes. For each sample and gene, we obtained read counts for the reference and alternate  
593 allele using *samtools* mpileup at the SNP loci for which the sample was heterozygous. We ran the 1-sample  
594 analysis on MBASED, obtained the major allele frequency and p-value of ASE for each gene, and applied

595 multiple test correction using Benjamini-Hochberg's method. As default, MBASED removed genes with less than  
596 10 reads for read depth. We determine a gene to display ASE if  $FDR \leq 0.05$  and major allele frequency  $\geq 0.6$ .

## 597 **Processing T2D loci**

598 We obtained the genomic coordinates of each of 380 fine-mapped T2D loci from Mahajan et al. (Mahajan et al.,  
599 2018) . For each SNP with  $PPA > 0$  in each locus, we extracted all its iPSC-PPC snATAC-seq peaks using  
600 *bedtools intersect* (Quinlan and Hall, 2010).

## 601 **Obtaining Roadmap and ENCODE epigenomic data**

602 We downloaded 15 chromHMM chromatin state annotations (Ernst and Kellis, 2012) in 127 tissues included in  
603 the Roadmap Epigenomics Program (Roadmap Epigenomics et al., 2015). Each state was predicted using a hidden  
604 Markov model (HMM) on the signal from five histone modification ChIP-seq experiments, including H3K4me3,  
605 H3K4me1, H3K36me3, H3K9me3 and H3K27me3. We obtained BED file from  
606 [https://egg2.wustl.edu/roadmap/web\\_portal/chr\\_state\\_learning.html](https://egg2.wustl.edu/roadmap/web_portal/chr_state_learning.html).

607 We downloaded H3K27ac peak coordinates for 192 tissues from the ENCODE data portal  
608 (<https://www.encodeproject.org/>) (Consortium, 2012; Davis et al., 2018). We selected all H3K27ac samples with  
609 NarrowPeak BED files that passed all quality filters established by ENCODE.

## 610 **Data availability**

611 iPSC-PPC scRNA-seq and snATAC-seq data was submitted to GEO: [GSE152610](#) (token *khyrckqqzpsrib*).  
612 Seurat objects, including snATAC-seq and scRNA-seq, results from differential gene expression, differential peak  
613 expression and motif enrichment analysis have been deposited to Figshare:  
614 [https://figshare.com/projects/Regulatory\\_variants\\_active\\_in\\_iPSC-](https://figshare.com/projects/Regulatory_variants_active_in_iPSC-)

615 [derived pancreatic progenitor cells are globally associated with Type 2 Diabetes in adults/119706](#). ESC-  
616 PPC reference scRNA-seq was obtained from GEO ([GSE114412](#)). ChromHMM chromatin states were obtained  
617 from [https://egg2.wustl.edu/roadmap/web\\_portal/chr\\_state\\_learning.html](https://egg2.wustl.edu/roadmap/web_portal/chr_state_learning.html). H3K27ac peak coordinates were  
618 obtained from <https://www.encodeproject.org/>. Fine mapped T2D loci were obtained from the Diagram  
619 Consortium (<https://www.diagram-consortium.org/>).

## 620 **Acknowledgements**

621 This work was supported in part by a California Institute for Regenerative Medicine (CIRM) grant GC1R-06673  
622 and NIH grants HG008118, HL107442, DK105541, and DK112155. JPN, TDA and MKRD were supported by  
623 the National Library of Medicine Training Grant T15LM011271. BS was supported by CIRM Bridges Stem Cell  
624 Research and Therapy Training Grant, Award #EDUC2-08375. We would like to thank Drs. Maike Sander, Bing  
625 Ren and Kyle Gaulton for insightful scientific conversations.

## 626 **Author information**

627 KAF, ADC, and MD conceived the study. ADC, KF and BMS performed iPSC-PPC differentiations. ADC  
628 generated the molecular data. JPN, MKRD, HM, MD, and TDA performed computational analysis. JPN and  
629 MKRD performed scRNA-seq data processing and analyses. HM, MD and JPN performed the snATAC-seq data  
630 processing and analyses. KAF oversaw the study. KAF, JPN, MKRD and MD prepared the manuscript.

## 631 **iPSCORE Consortium**

632 *University of California, San Diego, La Jolla, CA 92093, USA*

633 Angelo D. Arias, Timothy D. Arthur, Paola Benaglio, Matteo D'Antonio, Agnieszka D'Antonio-Chronowska,  
634 Christopher DeBoever, Margaret K.R. Donovan, Kelly A. Frazer, Olivier Harismendy, David Jakubosky, Kristen  
30

635 Jepsen, He Li, Hiroko Matsui, Naoki Nariai, Daniel T. O'Connor, Jennifer P. Nguyen, Fengwen Rao, Erin N.

636 Smith, William W. Young Greenwald

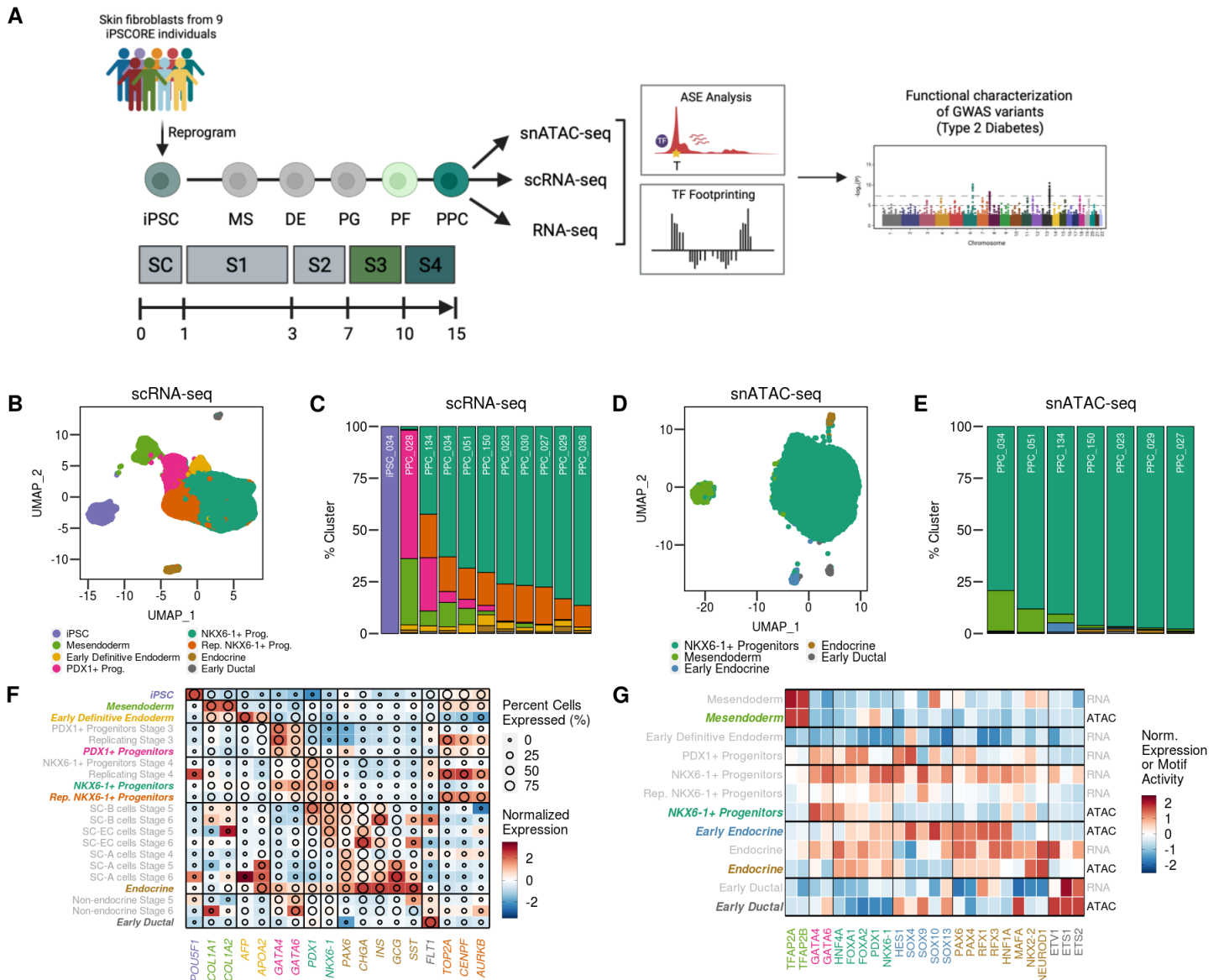
637 *Salk Institute for Biological Studies, La Jolla, CA 92037, USA*

638 Athanasia D. Panopoulos, W. Travis Berggren, Kenneth E. Diffenderfer

639

640 **Figures**

641 **Figure 1: iPSC-PPC are largely comprised of NKX6-1+ progenitors**



642

643

644

645

(A) Cartoon showing the overview design of the study. We differentiated iPSC-PPCs over a 15-day period and performed scRNA-seq, snATAC-seq, and bulk RNA-seq on matched samples and characterized regulatory variants for allele-specific effects on chromatin accessibility, transcription factor binding and gene expression.



646 Using these profiles, we discovered variants that are active within iPSC-PPC regulatory elements and are  
647 associated with Type 2 Diabetes.

648 (B) UMAP plot of scRNA-seq data from 83,871 single cells from one iPSC and ten iPSC-PPC samples. Each  
649 point represents a single cell color-coded by its assigned cluster.

650 (C) Stacked bar plot showing the fraction of cells from each sample assigned to each cluster in scRNA-seq. Color-  
651 coding corresponds to the clusters in panel B. Differentiations PPC029 and PPC036 were from the same iPSC  
652 clone.

653 (D) UMAP plot of snATAC-seq data from 25,654 single nuclei from seven iPSC-PPC samples. Each point  
654 represents a single nuclei color-coded by its assigned cluster.

655 (E) Stacked bar plot showing the fraction of cells from each sample assigned to each cluster in snATAC-seq.  
656 Color-coding corresponds to the clusters in panel D.

657 (F) Heatmap comparing the z-normalized expression of known marker genes between iPSC-PPC and cells from  
658 the reference ESC-PPC study. Color intensity corresponds to the mean z-normalized expression across all cell  
659 types, and the diameter corresponds to the fraction of cells expressing the markers above the threshold of 1% of  
660 the maximum expression value. Clusters labeled in italicized color correspond to the clusters in panel B. Clusters  
661 labeled in grey correspond to clusters identified in ESC-PPC scRNA-seq.

662 (G) Heatmap comparing the z-normalized motif activity scores from chromVAR for pancreatic-associated  
663 transcription factors in the snATAC-seq clusters from panel D. Also shown are the normalized expression of the  
664 pancreatic-associated transcription factors in the scRNA-seq clusters from panel B. Clusters labeled in italicized  
665 color correspond to the snATAC-seq clusters in panel D. Clusters labeled in grey correspond to the scRNA-seq  
666 clusters in panel B.

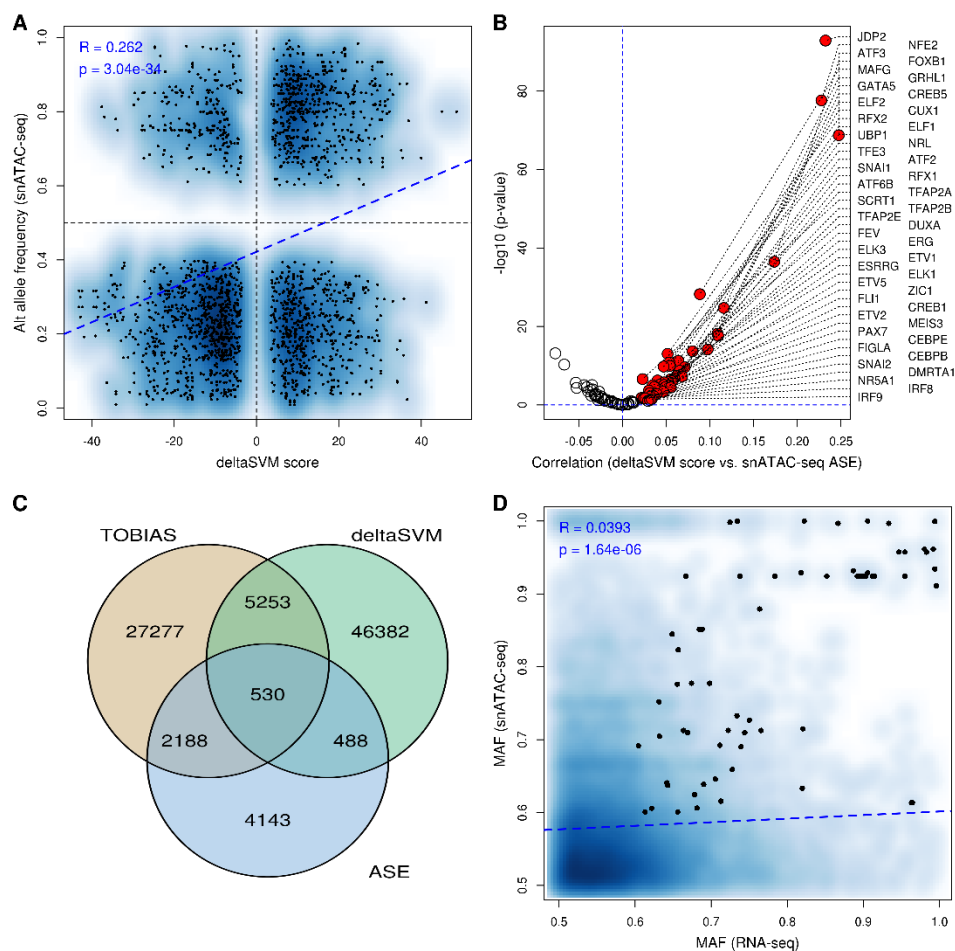
667

668

669

670

## Figure 2: Allele-specific effects of SNPs in iPSC-PPC snATAC-seq peaks



671

672

673

674

675

676

677

678

679

(A) Scatterplot showing a significantly positive correlation ( $R = 0.26$ ,  $p = 3.0 \times 10^{-34}$ ) between SNPs predicted to have allelic effects across all 94 transcription factors measured by deltaSVM (X axis) and the alternative allele frequency (from snATAC-seq ASE analysis, Y axis). The blue dashed line represents the regression line. When considering all the SNPs tested for ASE and deltaSVM, the correlation was significantly positive ( $R = 0.019$ ,  $p = 5.8 \times 10^{-80}$ ), indicating that deltaSVM accurately predicts the allelic effects of SNPs in snATAC-seq on transcription factor binding.

(B) Volcano plot showing the correlation between deltaSVM score and ASE measured by snATAC-seq. Each dot represents the correlation of all the SNPs for one of the 94 transcription factors tested by deltaSVM. Significant

680 positively correlated transcription factors are highlighted in red and their names are indicated on the right. The  
681 volcano plot shows that the distribution of correlation values is significantly skewed towards positive values,  
682 confirming that, in general, deltaSVM predictions are concordant with snATAC-seq ASE values.

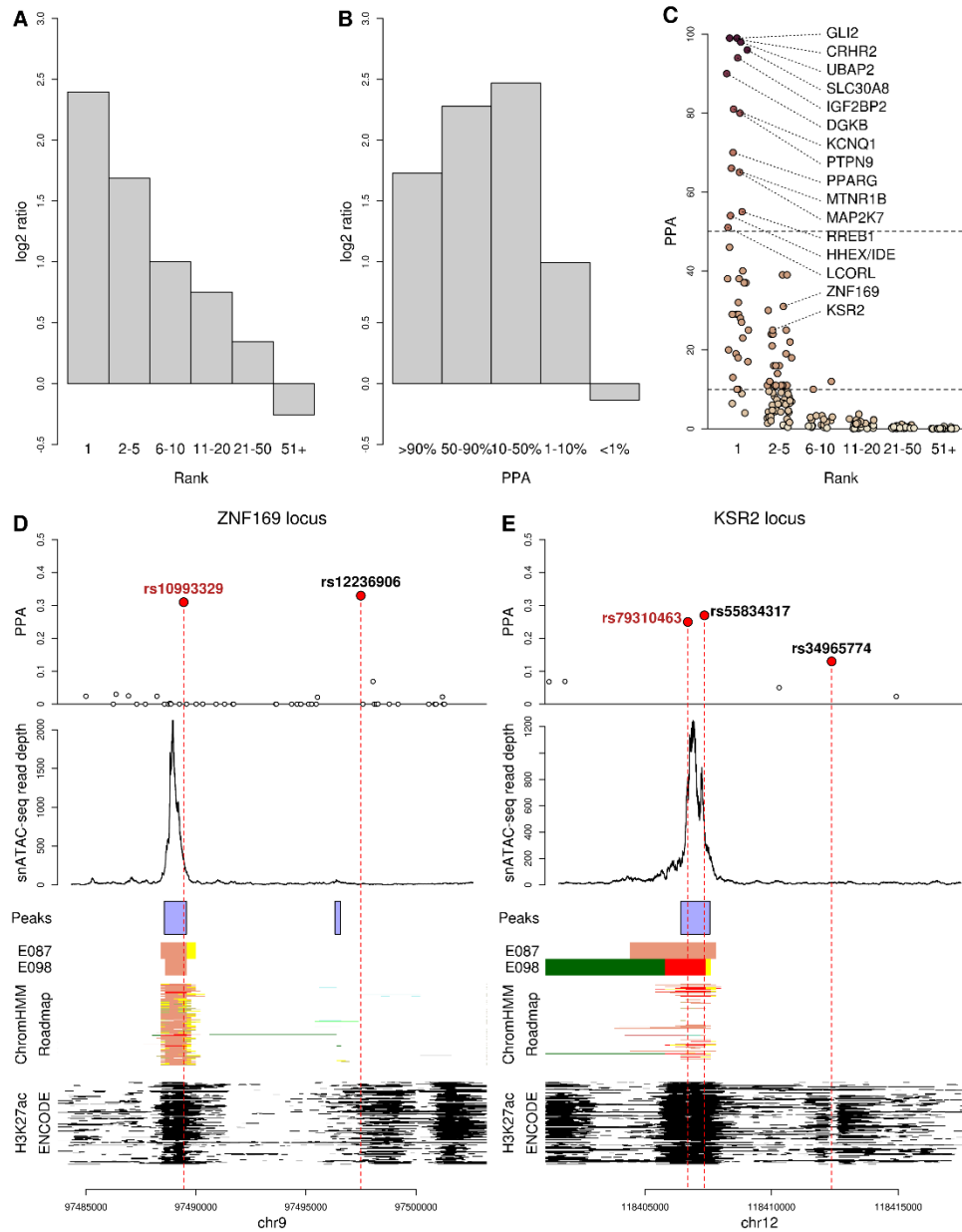
683 (C) Venn diagram showing the overlap between the three methods (TOBIAS, deltaSVM and ASE) to characterize  
684 the evidence of functional effects (transcription factor binding or allelic effects) for each variant.

685 (D) Smooth scatterplot showing a significant positive correlation ( $R = 0.039$ ,  $p = 1.6 \times 10^{-6}$ ) between the major  
686 allele frequency (MAF) of SNPs overlapping expressed genes, calculated by MBASED (X axis), and the MAF  
687 of SNPs overlapping snATAC-seq peaks at their corresponding promoters (Y axis). Dots represent genes with  
688 significant ASE that were associated with SNPs with ASE at their promoter. The blue dashed line represents the  
689 regression line.

690

691

### Figure 3: Associations between allele-specific effects and T2D-associated SNPs



692

693

694

695

696

697

(A, B) Barplots showing the enrichment for SNPs that overlap iPSC-PPC snATAC-seq peaks in T2D credible sets in different (A) rank or (B) PPA bins. X axis shows the rank or PPA bin and the Y axis represents the  $\log_2$  ratio between the proportion of SNPs overlapping peaks and the proportion of SNPs not overlapping peaks.

(C) Scatterplot showing the rank (X axis) and the PPA (Y axis: darker colors correspond to higher PPA values)

for the 209 T2D loci with SNPs that display allelic effects or overlap transcription factor binding sites. The index 37

698 genes associated with SNPs having  $PPA \geq 50\%$  and the index genes associated with the loci described in panels  
699 D and E are shown. Horizontal dashed lines represent  $PPA = 50\%$  and  $PPA = 10\%$ .

700 (D, E) Two T2D loci (D: ZNF169; and E: KSR2) where the top-ranked SNP does not overlap snATAC-seq peaks  
701 or is not associated with ASE. The scatterplot (top) shows the PPA of each SNP included in the 99% credible set.  
702 The SNPs described in the text are shown and the SNPs with ASE are indicated in maroon. The second plot from  
703 the top shows the read depth from snATAC-seq. Below are shown: iPSC-PPC snATAC-seq peak coordinates  
704 (purple); 15 chromHMM chromatin states for two pancreas samples (E087: pancreatic islets; E098: pancreas) and  
705 127 tissues included in Roadmap Epigenomics Program; and H3K27ac peak coordinates (in black) for 192 tissues  
706 obtained from the ENCODE data portal. Roadmap chromatin marks are colored as follows: 1) active TSS (red);  
707 2) flanking active TSS (orange-red); 3) transcription at gene 5' and 3' (lime green); 4) strong transcription (green);  
708 5) weak transcription (dark green); 6) genic enhancers (green-yellow); 7) enhancers (yellow); 8) ZNF genes and  
709 repeats (medium aquamarine); 9) heterochromatin (pale turquoise); 10) bivalent/poised enhancer or TSS (Indian  
710 red); 11) flanking bivalent/poised enhancer or TSS (dark salmon); 12) bivalent enhancer (dark khaki); 13)  
711 repressed polycomb (silver); 14) weak repressed polycomb (gainsboro); and 15) quiescent chromatin (white). In  
712 both examples, the SNPs with ASE overlap genomic regions that have H3K27ac peaks and are labeled as bivalent  
713 enhancers in many tissues. These examples show that the SNP with ASE, rather than the top-ranked SNP, is more  
714 likely to be functional and, therefore, causal for T2D.

## References

- (2019). Picard toolkit. Broad Institute, GitHub repository.
- Ait-Lounis, A., Baas, D., Barras, E., Benadiba, C., Charollais, A., Nlend Nlend, R., Liegeois, D., Meda, P., Durand, B., and Reith, W. (2007). Novel function of the ciliogenic transcription factor RFX3 in development of the endocrine pancreas. *Diabetes* *56*, 950-959.
- Alasoo, K., Rodrigues, J., Mukhopadhyay, S., Knights, A.J., Mann, A.L., Kundu, K., Consortium, H., Hale, C., Dougan, G., and Gaffney, D.J. (2018). Shared genetic effects on chromatin and gene expression indicate a role for enhancer priming in immune response. *Nat Genet* *50*, 424-431.
- Amemiya, H.M., Kundaje, A., and Boyle, A.P. (2019). The ENCODE Blacklist: Identification of Problematic Regions of the Genome. *Sci Rep* *9*, 9354.
- Baraille, F., Ayari, S., Carriere, V., Osinski, C., Garbin, K., Blondeau, B., Guillemain, G., Serradas, P., Rousset, M., Lacasa, M., *et al.* (2015). Glucose Tolerance Is Improved in Mice Invalidated for the Nuclear Receptor HNF-4gamma: A Critical Role for Enteroendocrine Cell Lineage. *Diabetes* *64*, 2744-2756.
- Bentsen, M., Goymann, P., Schultheis, H., Klee, K., Petrova, A., Wiegandt, R., Fust, A., Preussner, J., Kuenne, C., Braun, T., *et al.* (2020). ATAC-seq footprinting unravels kinetics of transcription factor binding during zygotic genome activation. *Nat Commun* *11*, 4267.
- Buniello, A., MacArthur, J.A.L., Cerezo, M., Harris, L.W., Hayhurst, J., Malangone, C., McMahon, A., Morales, J., Mountjoy, E., Sollis, E., *et al.* (2019). The NHGRI-EBI GWAS Catalog of published genome-wide association studies, targeted arrays and summary statistics 2019. *Nucleic Acids Res* *47*, D1005-D1012.
- Butler, A., Hoffman, P., Smibert, P., Papalex, E., and Satija, R. (2018). Integrating single-cell transcriptomic data across different conditions, technologies, and species. *Nat Biotechnol* *36*, 411-420.
- Cano, D.A., Soria, B., Martin, F., and Rojas, A. (2014). Transcriptional control of mammalian pancreas organogenesis. *Cell Mol Life Sci* *71*, 2383-2402.
- Chiou, J., Zeng, C., Cheng, Z., Han, J.Y., Schlichting, M., Miller, M., Mendez, R., Huang, S., Wang, J., Sui, Y., *et al.* (2021). Single-cell chromatin accessibility identifies pancreatic islet cell type- and state-specific regulatory programs of diabetes risk. *Nat Genet* *53*, 455-466.
- Consortium, E.P. (2012). An integrated encyclopedia of DNA elements in the human genome. *Nature* *489*, 57-74.
- D'Antonio-Chronowska, A., Donovan, M.K.R., Young Greenwald, W.W., Nguyen, J.P., Fujita, K., Hashem, S., Matsui, H., Soncin, F., Parast, M., Ward, M.C., *et al.* (2019). Association of Human iPSC Gene Signatures and X Chromosome Dosage with Two Distinct Cardiac Differentiation Trajectories. *Stem Cell Reports* *13*, 924-938.
- D'Antonio, M., Benaglio, P., Jakubosky, D., Greenwald, W.W., Matsui, H., Donovan, M.K.R., Li, H., Smith, E.N., D'Antonio-Chronowska, A., and Frazer, K.A. (2018). Insights into the Mutational Burden of Human Induced Pluripotent Stem Cells from an Integrative Multi-Omics Approach. *Cell Rep* *24*, 883-894.
- D'Antonio, M., Nguyen, J.P., Arthur, T.D., Matsui, H., Donovan, M.K.R., D'Antonio-Chronowska, A., and Frazer, K.A. (2021). In heart failure reactivation of RNA-binding proteins drives the transcriptome into a fetal state. *bioRxiv*, 2021.2004.2030.442191.
- Danecek, P., Bonfield, J.K., Liddle, J., Marshall, J., Ohan, V., Pollard, M.O., Whitwham, A., Keane, T., McCarthy, S.A., Davies, R.M., *et al.* (2021). Twelve years of SAMtools and BCFtools. *Gigascience* *10*.
- Davis, C.A., Hitz, B.C., Sloan, C.A., Chan, E.T., Davidson, J.M., Gabdank, I., Hilton, J.A., Jain, K., Baymuradov, U.K., Narayanan, A.K., *et al.* (2018). The Encyclopedia of DNA elements (ENCODE): data portal update. *Nucleic Acids Res* *46*, D794-D801.

760 DeBoever, C., Li, H., Jakubosky, D., Benaglio, P., Reyna, J., Olson, K.M., Huang, H., Biggs, W., Sandoval, E.,  
761 D'Antonio, M., *et al.* (2017). Large-Scale Profiling Reveals the Influence of Genetic Variation on Gene  
762 Expression in Human Induced Pluripotent Stem Cells. *Cell Stem Cell* 20, 533-546 e537.

763 DePristo, M.A., Banks, E., Poplin, R., Garimella, K.V., Maguire, J.R., Hartl, C., Philippakis, A.A., del Angel, G.,  
764 Rivas, M.A., Hanna, M., *et al.* (2011). A framework for variation discovery and genotyping using next-generation  
765 DNA sequencing data. *Nat Genet* 43, 491-498.

766 Dobin, A., Davis, C.A., Schlesinger, F., Drenkow, J., Zaleski, C., Jha, S., Batut, P., Chaisson, M., and Gingeras,  
767 T.R. (2013). STAR: ultrafast universal RNA-seq aligner. *Bioinformatics* 29, 15-21.

768 Doyle, M.J., and Sussel, L. (2007). Nkx2.2 regulates beta-cell function in the mature islet. *Diabetes* 56, 1999-  
769 2007.

770 Ernst, J., and Kellis, M. (2012). ChromHMM: automating chromatin-state discovery and characterization. *Nat*  
771 *Methods* 9, 215-216.

772 Fang, J., Jia, J., Makowski, M., Xu, M., Wang, Z., Zhang, T., Hoskins, J.W., Choi, J., Han, Y., Zhang, M., *et al.*  
773 (2017). Functional characterization of a multi-cancer risk locus on chr5p15.33 reveals regulation of TERT by  
774 ZNF148. *Nat Commun* 8, 15034.

775 Fazio, E.N., Young, C.C., Toma, J., Levy, M., Berger, K.R., Johnson, C.L., Mehmood, R., Swan, P., Chu, A.,  
776 Cregan, S.P., *et al.* (2017). Activating transcription factor 3 promotes loss of the acinar cell phenotype in response  
777 to cerulein-induced pancreatitis in mice. *Mol Biol Cell* 28, 2347-2359.

778 Feng, J., Liu, T., Qin, B., Zhang, Y., and Liu, X.S. (2012). Identifying ChIP-seq enrichment using MACS. *Nat*  
779 *Protoc* 7, 1728-1740.

780 Fornes, O., Castro-Mondragon, J.A., Khan, A., van der Lee, R., Zhang, X., Richmond, P.A., Modi, B.P., Correard,  
781 S., Gheorghe, M., Baranasic, D., *et al.* (2020). JASPAR 2020: update of the open-access database of transcription  
782 factor binding profiles. *Nucleic Acids Res* 48, D87-D92.

783 Gate, R.E., Cheng, C.S., Aiden, A.P., Siba, A., Tabaka, M., Lituiev, D., Machol, I., Gordon, M.G., Subramaniam,  
784 M., Shamim, M., *et al.* (2018). Genetic determinants of co-accessible chromatin regions in activated T cells across  
785 humans. *Nat Genet* 50, 1140-1150.

786 Genomes Project, C., Auton, A., Brooks, L.D., Durbin, R.M., Garrison, E.P., Kang, H.M., Korbel, J.O., Marchini,  
787 J.L., McCarthy, S., McVean, G.A., *et al.* (2015). A global reference for human genetic variation. *Nature* 526, 68-  
788 74.

789 Geusz, R.J., Wang, A., Chiou, J., Lnacman, J.J., Wetton, N., Kefalopoulou, S., Wang, J., Qiu, Y., Yan, J., Aylward,  
790 A., *et al.* (2020). Pancreatic progenitor epigenome maps prioritize type 2 diabetes risk genes with roles in  
791 development. *BioRxiv*.

792 Ghandi, M., Lee, D., Mohammad-Noori, M., and Beer, M.A. (2014). Enhanced regulatory sequence prediction  
793 using gapped k-mer features. *PLoS Comput Biol* 10, e1003711.

794 Ghandi, M., Mohammad-Noori, M., Ghareghani, N., Lee, D., Garraway, L., and Beer, M.A. (2016). gkmSVM:  
795 an R package for gapped-kmer SVM. *Bioinformatics* 32, 2205-2207.

796 Giambartolomei, C., Vukcevic, D., Schadt, E.E., Franke, L., Hingorani, A.D., Wallace, C., and Plagnol, V. (2014).  
797 Bayesian test for colocalisation between pairs of genetic association studies using summary statistics. *PLoS Genet*  
798 *10*, e1004383.

799 Giambartolomei, C., Zhenli Liu, J., Zhang, W., Hauberg, M., Shi, H., Boocock, J., Pickrell, J., Jaffe, A.E.,  
800 CommonMind, C., Pasaniuc, B., *et al.* (2018). A Bayesian framework for multiple trait colocalization from  
801 summary association statistics. *Bioinformatics* 34, 2538-2545.

802 Greenwald, W.W., Chiou, J., Yan, J., Qiu, Y., Dai, N., Wang, A., Nariai, N., Aylward, A., Han, J.Y., Kadakia,  
803 N., *et al.* (2019). Pancreatic islet chromatin accessibility and conformation reveals distal enhancer networks of  
804 type 2 diabetes risk. *Nat Commun* 10, 2078.



- 805 Gupta, D., Kono, T., and Evans-Molina, C. (2010). The role of peroxisome proliferator-activated receptor gamma  
806 in pancreatic beta cell function and survival: therapeutic implications for the treatment of type 2 diabetes mellitus.  
807 *Diabetes Obes Metab* 12, 1036-1047.
- 808 Harrow, J., Frankish, A., Gonzalez, J.M., Tapanari, E., Diekhans, M., Kokocinski, F., Aken, B.L., Barrell, D.,  
809 Zadissa, A., Searle, S., *et al.* (2012). GENCODE: the reference human genome annotation for The ENCODE  
810 Project. *Genome Res* 22, 1760-1774.
- 811 Hess, D.A., Humphrey, S.E., Ishibashi, J., Damsz, B., Lee, A.H., Glimcher, L.H., and Konieczny, S.F. (2011).  
812 Extensive pancreas regeneration following acinar-specific disruption of Xbp1 in mice. *Gastroenterology* 141,  
813 1463-1472.
- 814 Huang, Y.C., Hasegawa, H., Wang, S.W., Ku, C.C., Lin, Y.C., Chiou, S.S., Hou, M.F., Wu, D.C., Tsai, E.M.,  
815 Saito, S., *et al.* (2011). Jun dimerization protein 2 controls senescence and differentiation via regulating histone  
816 modification. *J Biomed Biotechnol* 2011, 569034.
- 817 Ishigaki, K., Akiyama, M., Kanai, M., Takahashi, A., Kawakami, E., Sugishita, H., Sakaue, S., Matoba, N., Low,  
818 S.K., Okada, Y., *et al.* (2020). Large-scale genome-wide association study in a Japanese population identifies  
819 novel susceptibility loci across different diseases. *Nat Genet* 52, 669-679.
- 820 Itkin-Ansari, P., Marcora, E., Geron, I., Tyrberg, B., Demeterco, C., Hao, E., Padilla, C., Ratineau, C., Leiter, A.,  
821 Lee, J.E., *et al.* (2005). NeuroD1 in the endocrine pancreas: localization and dual function as an activator and  
822 repressor. *Dev Dyn* 233, 946-953.
- 823 Jakubosky, D., D'Antonio, M., Bonder, M.J., Smail, C., Donovan, M.K.R., Young Greenwald, W.W., Matsui, H.,  
824 i, Q.T.L.C., D'Antonio-Chronowska, A., Stegle, O., *et al.* (2020a). Properties of structural variants and short  
825 tandem repeats associated with gene expression and complex traits. *Nat Commun* 11, 2927.
- 826 Jakubosky, D., Smith, E.N., D'Antonio, M., Jan Bonder, M., Young Greenwald, W.W., D'Antonio-Chronowska,  
827 A., Matsui, H., i, Q.T.L.C., Stegle, O., Montgomery, S.B., *et al.* (2020b). Discovery and quality analysis of a  
828 comprehensive set of structural variants and short tandem repeats. *Nat Commun* 11, 2928.
- 829 Jennings, R.E., Berry, A.A., Strutt, J.P., Gerrard, D.T., and Hanley, N.A. (2015). Human pancreas development.  
830 *Development* 142, 3126-3137.
- 831 Kang, H.M., Subramaniam, M., Targ, S., Nguyen, M., Maliskova, L., McCarthy, E., Wan, E., Wong, S., Byrnes,  
832 L., Lanata, C.M., *et al.* (2018). Multiplexed droplet single-cell RNA-sequencing using natural genetic variation.  
833 *Nat Biotechnol* 36, 89-94.
- 834 Kobberup, S., Nyeng, P., Juhl, K., Hutton, J., and Jensen, J. (2007). ETS-family genes in pancreatic development.  
835 *Dev Dyn* 236, 3100-3110.
- 836 Kojayan, G.G., Alizadeh, R.F., Li, S., and Ichii, H. (2019). Reducing Pancreatic Fibrosis Using Antioxidant  
837 Therapy Targeting Nrf2 Antioxidant Pathway: A Possible Treatment for Chronic Pancreatitis. *Pancreas* 48, 1259-  
838 1262.
- 839 Li, B., and Dewey, C.N. (2011). RSEM: accurate transcript quantification from RNA-Seq data with or without a  
840 reference genome. *BMC Bioinformatics* 12, 323.
- 841 Li, H., and Durbin, R. (2009). Fast and accurate short read alignment with Burrows-Wheeler transform.  
842 *Bioinformatics* 25, 1754-1760.
- 843 Li, L., Li, Y., Timothy Sembiring Meliala, I., Kasim, V., and Wu, S. (2020). Biological roles of Yin Yang 2: Its  
844 implications in physiological and pathological events. *J Cell Mol Med* 24, 12886-12899.
- 845 Lioubinski, O., Muller, M., Wegner, M., and Sander, M. (2003). Expression of Sox transcription factors in the  
846 developing mouse pancreas. *Dev Dyn* 227, 402-408.
- 847 Ma, Y., Wang, X., Peng, Y., and Ding, X. (2016). Forkhead box O1 promotes INS1 cell apoptosis by reducing  
848 the expression of CD24. *Mol Med Rep* 13, 2991-2998.
- 849 Mahajan, A., Taliun, D., Thurner, M., Robertson, N.R., Torres, J.M., Rayner, N.W., Payne, A.J., Steinthorsdottir,  
850 V., Scott, R.A., Grarup, N., *et al.* (2018). Fine-mapping type 2 diabetes loci to single-variant resolution using  
851 high-density imputation and islet-specific epigenome maps. *Nat Genet* 50, 1505-1513.

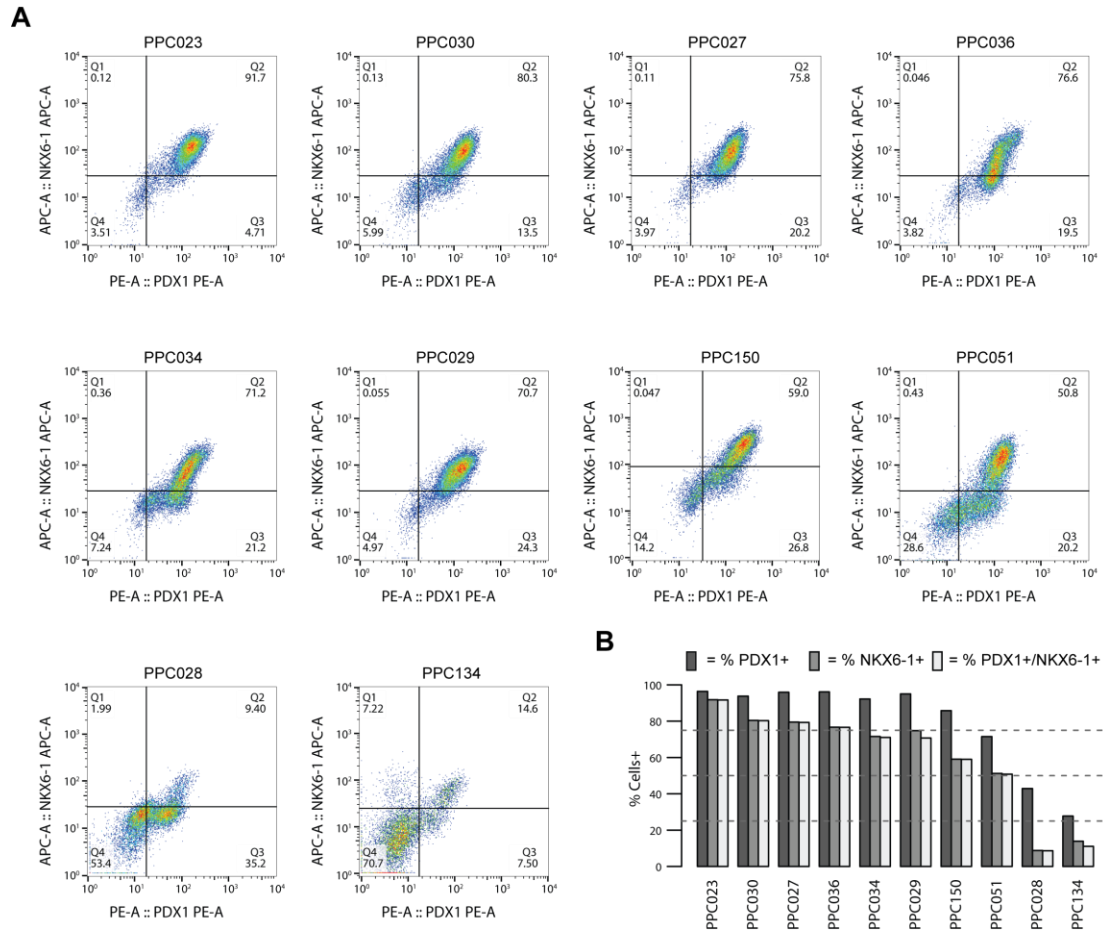
- 852 Majumdar, A., Haldar, T., Bhattacharya, S., and Witte, J.S. (2018). An efficient Bayesian meta-analysis approach  
853 for studying cross-phenotype genetic associations. *PLoS Genet* *14*, e1007139.
- 854 Mastracci, T.L., Anderson, K.R., Papizan, J.B., and Sussel, L. (2013). Regulation of Neurod1 contributes to the  
855 lineage potential of Neurogenin3+ endocrine precursor cells in the pancreas. *PLoS Genet* *9*, e1003278.
- 856 Mayba, O., Gilbert, H.N., Liu, J., Haverty, P.M., Jhunjhunwala, S., Jiang, Z., Watanabe, C., and Zhang, Z. (2014).  
857 MBASED: allele-specific expression detection in cancer tissues and cell lines. *Genome Biol* *15*, 405.
- 858 McKenna, A., Hanna, M., Banks, E., Sivachenko, A., Cibulskis, K., Kernysky, A., Garimella, K., Altshuler, D.,  
859 Gabriel, S., Daly, M., *et al.* (2010). The Genome Analysis Toolkit: a MapReduce framework for analyzing next-  
860 generation DNA sequencing data. *Genome Res* *20*, 1297-1303.
- 861 Miyazaki, S., Taniguchi, H., Moritoh, Y., Tashiro, F., Yamamoto, T., Yamato, E., Ikegami, H., Ozato, K., and  
862 Miyazaki, J. (2010). Nuclear hormone retinoid X receptor (RXR) negatively regulates the glucose-stimulated  
863 insulin secretion of pancreatic  $\beta$ -cells. *Diabetes* *59*, 2854-2861.
- 864 Nakai, A., Tanabe, M., Kawazoe, Y., Inazawa, J., Morimoto, R.I., and Nagata, K. (1997). HSF4, a new member  
865 of the human heat shock factor family which lacks properties of a transcriptional activator. *Mol Cell Biol* *17*, 469-  
866 481.
- 867 Nowotschin, S., Setty, M., Kuo, Y.Y., Liu, V., Garg, V., Sharma, R., Simon, C.S., Saiz, N., Gardner, R., Boutet,  
868 S.C., *et al.* (2019). The emergent landscape of the mouse gut endoderm at single-cell resolution. *Nature* *569*, 361-  
869 367.
- 870 Oh, S., Shao, J., Mitra, J., Xiong, F., D'Antonio, M., Wang, R., Garcia-Bassets, I., Ma, Q., Zhu, X., Lee, J.H., *et*  
871 *al.* (2021). Enhancer release and retargeting activates disease-susceptibility genes. *Nature* *595*, 735-740.
- 872 Pagliuca, F.W., Millman, J.R., Gurtler, M., Segel, M., Van Dervort, A., Ryu, J.H., Peterson, Q.P., Greiner, D.,  
873 and Melton, D.A. (2014). Generation of functional human pancreatic beta cells in vitro. *Cell* *159*, 428-439.
- 874 Panopoulos, A.D., D'Antonio, M., Benaglio, P., Williams, R., Hashem, S.I., Schuldt, B.M., DeBoever, C., Arias,  
875 A.D., Garcia, M., Nelson, B.C., *et al.* (2017). iPSCORE: A Resource of 222 iPSC Lines Enabling Functional  
876 Characterization of Genetic Variation across a Variety of Cell Types. *Stem Cell Reports* *8*, 1086-1100.
- 877 Pennacchio, L.A., Bickmore, W., Dean, A., Nobrega, M.A., and Bejerano, G. (2013). Enhancers: five essential  
878 questions. *Nat Rev Genet* *14*, 288-295.
- 879 Pickrell, J.K. (2014). Joint analysis of functional genomic data and genome-wide association studies of 18 human  
880 traits. *Am J Hum Genet* *94*, 559-573.
- 881 Pictet, R.L., Clark, W.R., Williams, R.H., and Rutter, W.J. (1972). An ultrastructural analysis of the developing  
882 embryonic pancreas. *Dev Biol* *29*, 436-467.
- 883 Purcell, S., Neale, B., Todd-Brown, K., Thomas, L., Ferreira, M.A., Bender, D., Maller, J., Sklar, P., de Bakker,  
884 P.I., Daly, M.J., *et al.* (2007). PLINK: a tool set for whole-genome association and population-based linkage  
885 analyses. *Am J Hum Genet* *81*, 559-575.
- 886 Quinlan, A.R., and Hall, I.M. (2010). BEDTools: a flexible suite of utilities for comparing genomic features.  
887 *Bioinformatics* *26*, 841-842.
- 888 Raap, M., Gierendt, L., Kreipe, H.H., and Christgen, M. (2021). Transcription factor AP-2beta in development,  
889 differentiation and tumorigenesis. *Int J Cancer* *149*, 1221-1227.
- 890 Rai, V., Quang, D.X., Erdos, M.R., Cusanovich, D.A., Daza, R.M., Narisu, N., Zou, L.S., Didion, J.P., Guan, Y.,  
891 Shendure, J., *et al.* (2020). Single-cell ATAC-Seq in human pancreatic islets and deep learning upscaling of rare  
892 cells reveals cell-specific type 2 diabetes regulatory signatures. *Mol Metab* *32*, 109-121.
- 893 Reichert, M., and Rustgi, A.K. (2011). Pancreatic ductal cells in development, regeneration, and neoplasia. *J Clin*  
894 *Invest* *121*, 4572-4578.
- 895 Rezania, A., Bruin, J.E., Arora, P., Rubin, A., Batushansky, I., Asadi, A., O'Dwyer, S., Quiskamp, N., Mojibian,  
896 M., Albrecht, T., *et al.* (2014). Reversal of diabetes with insulin-producing cells derived in vitro from human  
897 pluripotent stem cells. *Nat Biotechnol* *32*, 1121-1133.

- 898 Ripka, S., Neesse, A., Riedel, J., Bug, E., Aigner, A., Poulosom, R., Fulda, S., Neoptolemos, J., Greenhalf, W.,  
899 Barth, P., *et al.* (2010). CUX1: target of Akt signalling and mediator of resistance to apoptosis in pancreatic  
900 cancer. *Gut* *59*, 1101-1110.
- 901 Roadmap Epigenomics, C., Kundaje, A., Meuleman, W., Ernst, J., Bilenky, M., Yen, A., Heravi-Moussavi, A.,  
902 Kheradpour, P., Zhang, Z., Wang, J., *et al.* (2015). Integrative analysis of 111 reference human epigenomes.  
903 *Nature* *518*, 317-330.
- 904 Sakai, T., Mashima, H., Yamada, Y., Goto, T., Sato, W., Dohmen, T., Kamada, K., Yoshioka, M., Uchinami, H.,  
905 Yamamoto, Y., *et al.* (2014). The roles of interferon regulatory factors 1 and 2 in the progression of human  
906 pancreatic cancer. *Pancreas* *43*, 909-916.
- 907 Sakikubo, M., Furuyama, K., Horiguchi, M., Hosokawa, S., Aoyama, Y., Tsuboi, K., Goto, T., Hirata, K., Masui,  
908 T., Dor, Y., *et al.* (2018). Ptf1a inactivation in adult pancreatic acinar cells causes apoptosis through activation of  
909 the endoplasmic reticulum stress pathway. *Sci Rep* *8*, 15812.
- 910 Saykali, B., Mathiah, N., Nahaboo, W., Racu, M.L., Hammou, L., Defrance, M., and Migeotte, I. (2019). Distinct  
911 mesoderm migration phenotypes in extra-embryonic and embryonic regions of the early mouse embryo. *Elife* *8*.
- 912 Schep, A.N., Wu, B., Buenrostro, J.D., and Greenleaf, W.J. (2017). chromVAR: inferring transcription-factor-  
913 associated accessibility from single-cell epigenomic data. *Nat Methods* *14*, 975-978.
- 914 Shahjalal, H.M., Abdal Dayem, A., Lim, K.M., Jeon, T.I., and Cho, S.G. (2018). Generation of pancreatic beta  
915 cells for treatment of diabetes: advances and challenges. *Stem Cell Res Ther* *9*, 355.
- 916 Sobel, J., Guay, C., Elhanani, O., Rodriguez-Trejo, A., Stoll, L., Menoud, V., Jacovetti, C., Walker, M.D., and  
917 Regazzi, R. (2021). Scrt1, a transcriptional regulator of beta-cell proliferation identified by differential chromatin  
918 accessibility during islet maturation. *Sci Rep* *11*, 8800.
- 919 Stormo, G.D. (2013). Modeling the specificity of protein-DNA interactions. *Quant Biol* *1*, 115-130.
- 920 Suzuki, K., Akiyama, M., Ishigaki, K., Kanai, M., Hosoe, J., Shojima, N., Hozawa, A., Kadota, A., Kuriki, K.,  
921 Naito, M., *et al.* (2019). Identification of 28 new susceptibility loci for type 2 diabetes in the Japanese population.  
922 *Nat Genet* *51*, 379-386.
- 923 Syafruddin, S.E., Ling, S., Low, T.Y., and Mohtar, M.A. (2021). More Than Meets the Eye: Revisiting the Roles  
924 of Heat Shock Factor 4 in Health and Diseases. *Biomolecules* *11*.
- 925 Teo, A.K., Tsuneyoshi, N., Hoon, S., Tan, E.K., Stanton, L.W., Wright, C.V., and Dunn, N.R. (2015). PDX1  
926 binds and represses hepatic genes to ensure robust pancreatic commitment in differentiating human embryonic  
927 stem cells. *Stem Cell Reports* *4*, 578-590.
- 928 Thurner, M., van de Bunt, M., Torres, J.M., Mahajan, A., Nylander, V., Bennett, A.J., Gaulton, K.J., Barrett, A.,  
929 Burrows, C., Bell, C.G., *et al.* (2018). Integration of human pancreatic islet genomic data refines regulatory  
930 mechanisms at Type 2 Diabetes susceptibility loci. *Elife* *7*.
- 931 Van der Auwera, G.A., Carneiro, M.O., Hartl, C., Poplin, R., Del Angel, G., Levy-Moonshine, A., Jordan, T.,  
932 Shakir, K., Roazen, D., Thibault, J., *et al.* (2013). From FastQ data to high confidence variant calls: the Genome  
933 Analysis Toolkit best practices pipeline. *Curr Protoc Bioinformatics* *43*, 11 10 11-11 10 33.
- 934 Varshney, A., Scott, L.J., Welch, R.P., Erdos, M.R., Chines, P.S., Narisu, N., Albanus, R.D., Orchard, P.,  
935 Wolford, B.N., Kursawe, R., *et al.* (2017). Genetic regulatory signatures underlying islet gene expression and  
936 type 2 diabetes. *Proc Natl Acad Sci U S A* *114*, 2301-2306.
- 937 Veres, A., Faust, A.L., Bushnell, H.L., Engquist, E.N., Kenty, J.H., Harb, G., Poh, Y.C., Sintov, E., Gurtler, M.,  
938 Pagliuca, F.W., *et al.* (2019). Charting cellular identity during human in vitro beta-cell differentiation. *Nature*  
939 *569*, 368-373.
- 940 Vinuela, A., Varshney, A., van de Bunt, M., Prasad, R.B., Asplund, O., Bennett, A., Boehnke, M., Brown, A.A.,  
941 Erdos, M.R., Fadista, J., *et al.* (2020). Genetic variant effects on gene expression in human pancreatic islets and  
942 their implications for T2D. *Nat Commun* *11*, 4912.

- 943 Vujkovic, M., Keaton, J.M., Lynch, J.A., Miller, D.R., Zhou, J., Tcheandjieu, C., Huffman, J.E., Assimes, T.L.,  
944 Lorenz, K., Zhu, X., *et al.* (2020). Discovery of 318 new risk loci for type 2 diabetes and related vascular outcomes  
945 among 1.4 million participants in a multi-ancestry meta-analysis. *Nat Genet* 52, 680-691.
- 946 Wallace, C. (2020). Eliciting priors and relaxing the single causal variant assumption in colocalisation analyses.  
947 *PLoS Genet* 16, e1008720.
- 948 Wang, J., Kilic, G., Aydin, M., Burke, Z., Oliver, G., and Sosa-Pineda, B. (2005). Prox1 activity controls pancreas  
949 morphogenesis and participates in the production of "secondary transition" pancreatic endocrine cells. *Dev Biol*  
950 286, 182-194.
- 951 Wang, W.D., Melville, D.B., Montero-Balaguer, M., Hatzopoulos, A.K., and Knapik, E.W. (2011). Tfp2a and  
952 Foxd3 regulate early steps in the development of the neural crest progenitor population. *Dev Biol* 360, 173-185.
- 953 Xu, E.E., Krentz, N.A., Tan, S., Chow, S.Z., Tang, M., Nian, C., and Lynn, F.C. (2015). SOX4 cooperates with  
954 neurogenin 3 to regulate endocrine pancreas formation in mouse models. *Diabetologia* 58, 1013-1023.
- 955 Xuan, S., and Sussel, L. (2016). GATA4 and GATA6 regulate pancreatic endoderm identity through inhibition  
956 of hedgehog signaling. *Development* 143, 780-786.
- 957 Yamagata, K. (2014). Roles of HNF1alpha and HNF4alpha in pancreatic beta-cells: lessons from a monogenic  
958 form of diabetes (MODY). *Vitam Horm* 95, 407-423.
- 959 Yan, J., Qiu, Y., Ribeiro Dos Santos, A.M., Yin, Y., Li, Y.E., Vinckier, N., Nariai, N., Benaglio, P., Raman, A.,  
960 Li, X., *et al.* (2021). Systematic analysis of binding of transcription factors to noncoding variants. *Nature* 591,  
961 147-151.
- 962 Yu, C., Cui, S., Zong, C., Gao, W., Xu, T., Gao, P., Chen, J., Qin, D., Guan, Q., Liu, Y., *et al.* (2015). The Orphan  
963 Nuclear Receptor NR4A1 Protects Pancreatic beta-Cells from Endoplasmic Reticulum (ER) Stress-mediated  
964 Apoptosis. *J Biol Chem* 290, 20687-20699.

## SUPPLEMENTAL FIGURES

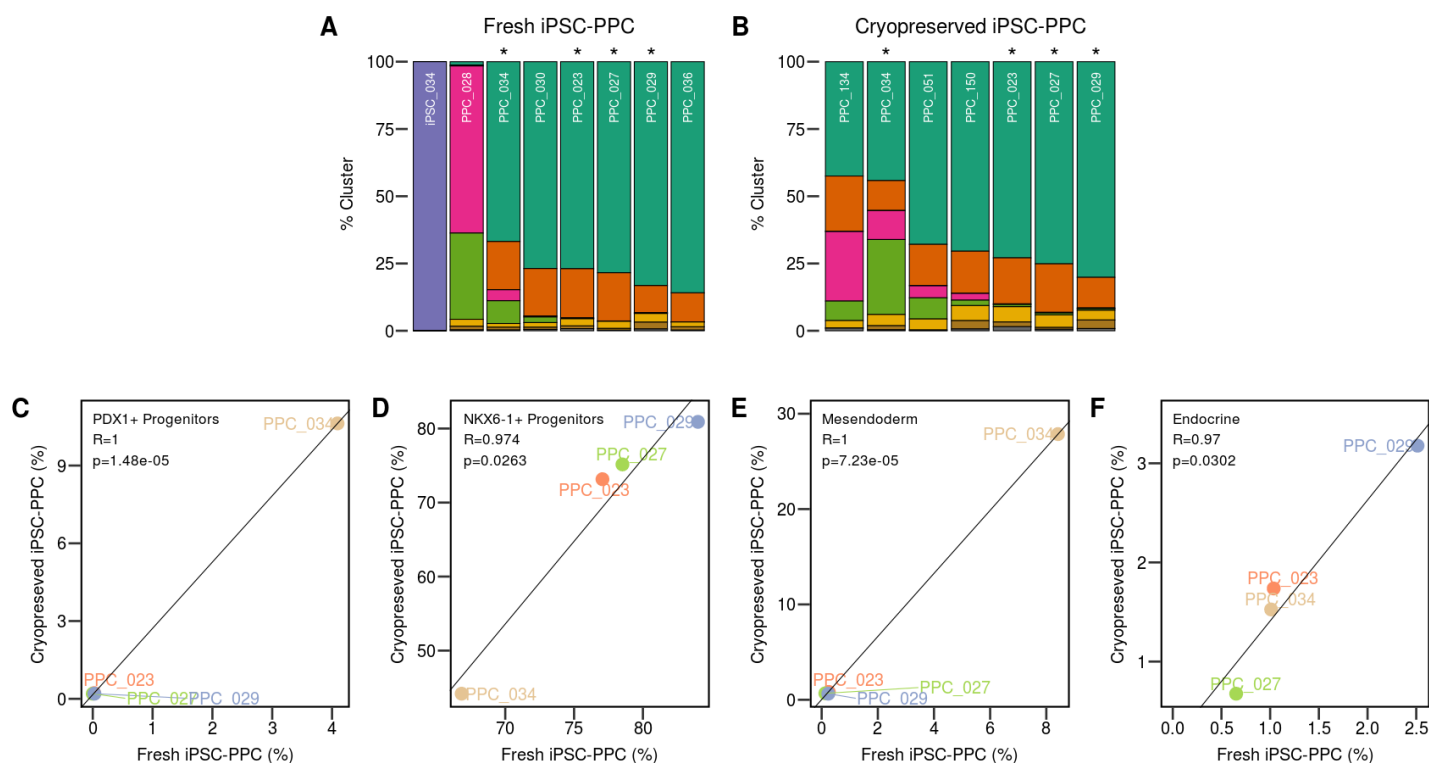
**Figure S1: Measurement of PDX1-positive and NKX6-1-positive cells by flow cytometry**



(A) Flow cytometry analysis at D15 of ten iPSC-PPC differentiations. The fraction of cells stained for PPC markers, PDX1 and NKX6-1, were measured. Differentiations PPC029 and PPC036 were from the same iPSC clone.

(B) Bar plot showing the fraction of iPSC-PPC cells positively stained for PPC markers, *PDX1* and *NKX6-1*, and positive for both *PDX1* and *NKX6-1*. Differentiations PPC029 and PPC036 were from the same iPSC clone.

## Figure S2: Similar cell type proportions between fresh and cryopreserved cells



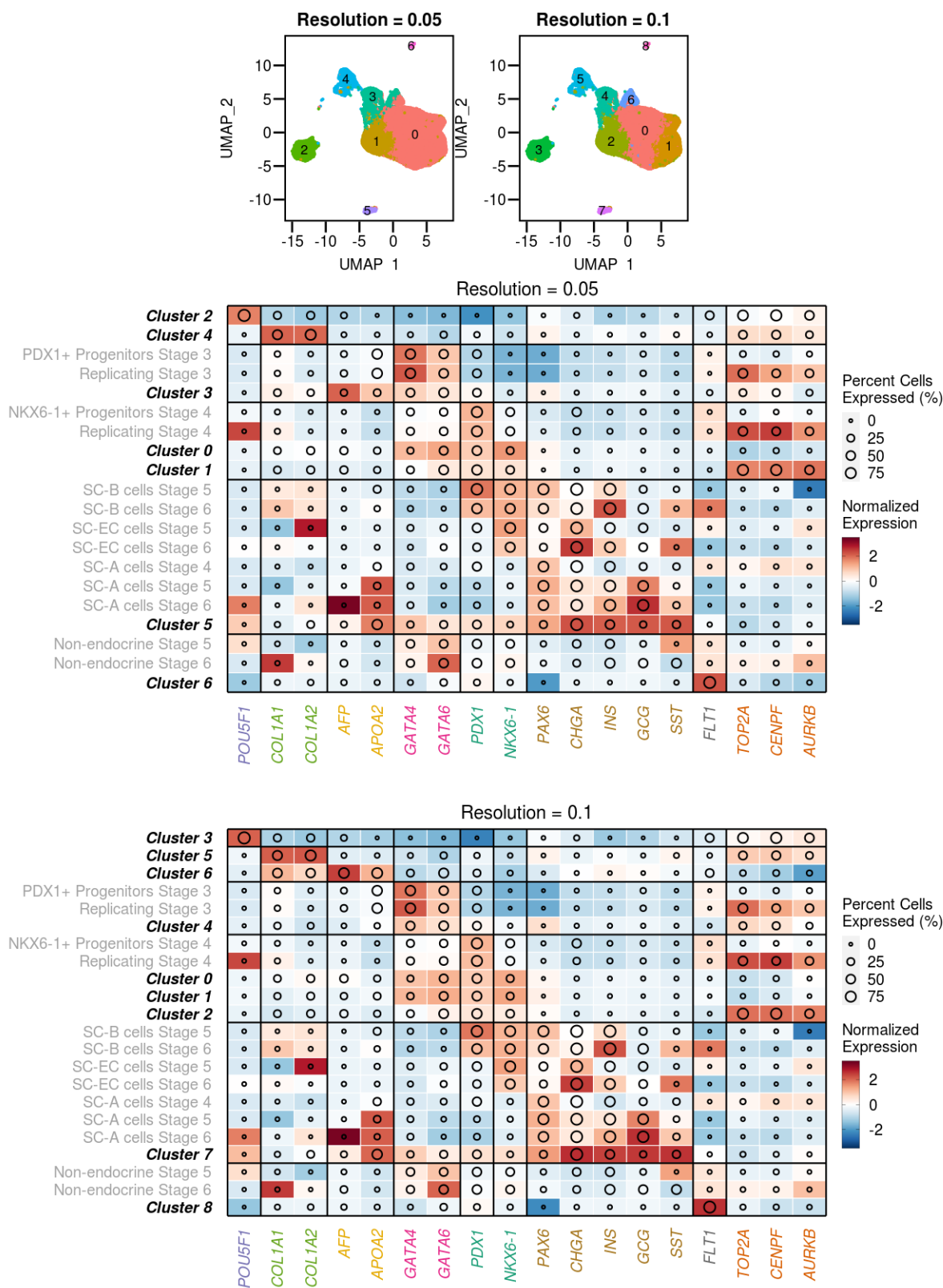
To determine if cryopreservation influences our detection of iPSC-PPC cell types, we integrated scRNA-seq obtained from eight fresh (i.e., not frozen) sample preparations (seven iPSC-PPC and one iPSC sample, aggregated into a single pool) with two pools of four and three cryopreserved iPSC-PPC samples. To assign the sample identity of each cell in the two cryopreserved pools, we performed sample deconvolution with demuxlet using genotype information from whole genome sequencing of nine individuals (DeBoever et al., 2017), two of which served as negative controls (i.e. samples from these two individuals were not included in the cryopreserved pools, Table S1). For the fresh preparations, each sample was processed independently from the others, therefore deconvolution using Demuxlet (Kang et al., 2018) was not required. For each of the four iPSC-PPC samples with matched fresh and cryopreserved preparations (indicated by the asterisks above the bar plots), we compared the proportions of cells in PDX1+ progenitors, NKX6-1+ progenitors, mesendoderm, and endocrine, and found that fresh and cryopreserved samples were highly correlated. These results indicate that fresh and cryopreserved cells can be used interchangeably to characterize the cellular composition of iPSC-PPC. The figure shows:

(A) Stacked bar plots showing the fraction of cells from each fresh iPSC-PPC sample assigned to each cell type using the same color coding as Figure 1B. Asterisks indicates the four iPSC-PPC samples with matched fresh and cryopreserved preparations.

(B) Stacked bar plots showing the fraction of cells from each cryopreserved iPSC-PPC sample assigned to each cell type using the same color coding as Figure 1B.

(C-F) For the four iPSC-PPC samples with matched fresh and cryopreserved samples, we show the association between each preparation by comparing the fraction of cells for (C) PDX1+ progenitors, (D) NKX6-1+ progenitors, (E) mesendoderm and (F) endocrine.

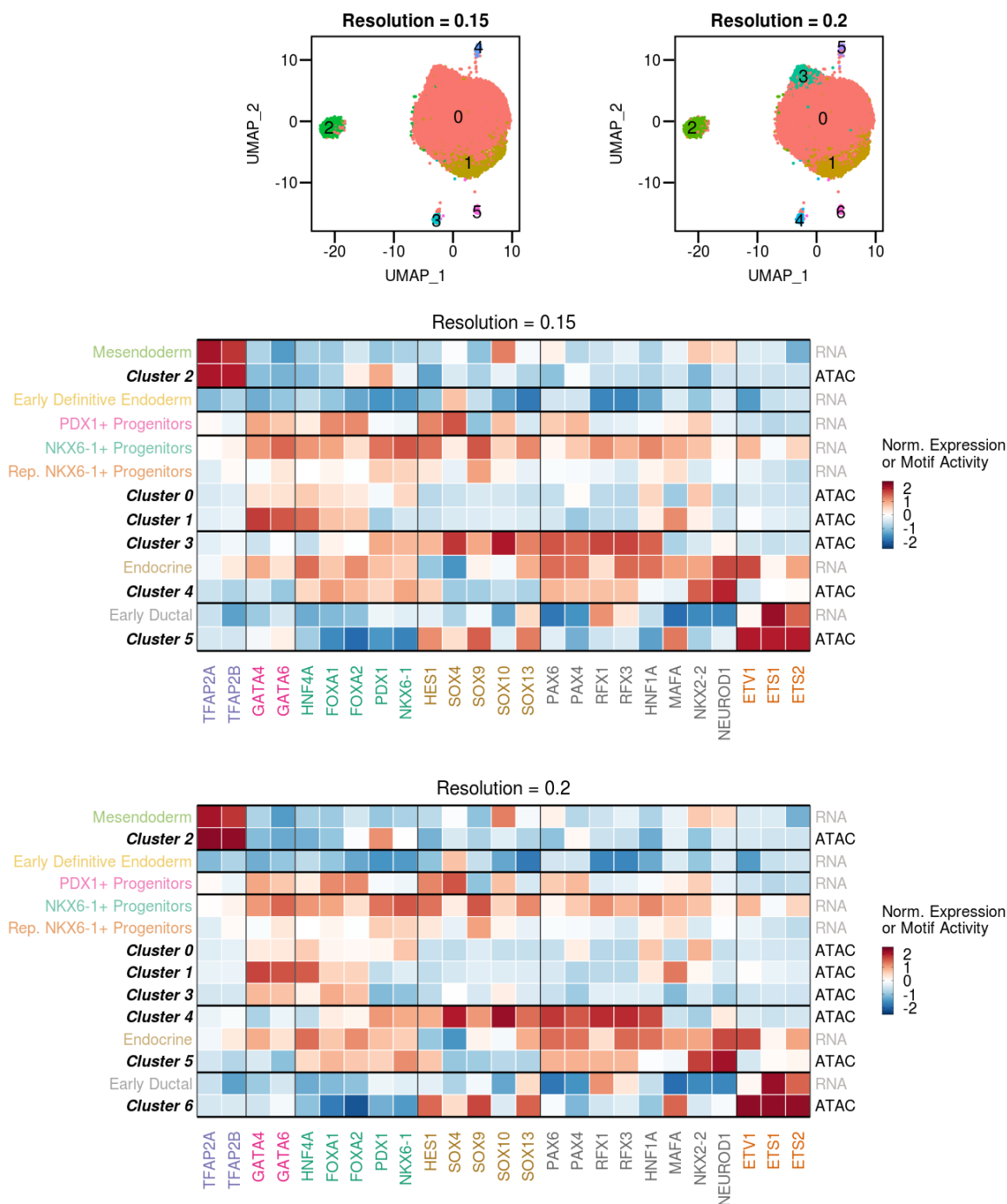
### Figure S3: Clustering of iPSC-PPC scRNA-seq at two additional resolutions





Clustering was performed on 83,971 single cells from one iPSC and ten iPSC-PPC samples at resolutions 0.05, 0.08 (shown in Figure 1B) and 0.1. With increasing resolution, we found that cluster 0 (*NKX6-1*+ progenitors) was further divided into subclusters. While all subclusters expressed *PDX1* and *NKX6-1*, one cluster expressed cell division markers (*TOP2A*, *CENPF*, and *AURKB*) at high levels, indicating that this cluster consists of replicating *NKX6-1*+ progenitors. Because the expression profiles are similar between the subclusters within cluster 0 at resolution 0.1, we used resolution 0.08 for downstream analyses where the subclusters were collapsed to form *NKX6-1*+ progenitors (Figure 1B). Red-to-blue shade in the heatmaps indicates z-normalized expression and the diameter represents the fraction of cells that express 1% of the maximal expression within that cell type. Cluster labels in black correspond to clusters in iPSC-PPC scRNA-seq (shown in the UMAP plots above the heatmaps). Cluster labels in grey correspond to clusters identified ESC-PPC scRNA-seq (Veres et al., 2019).

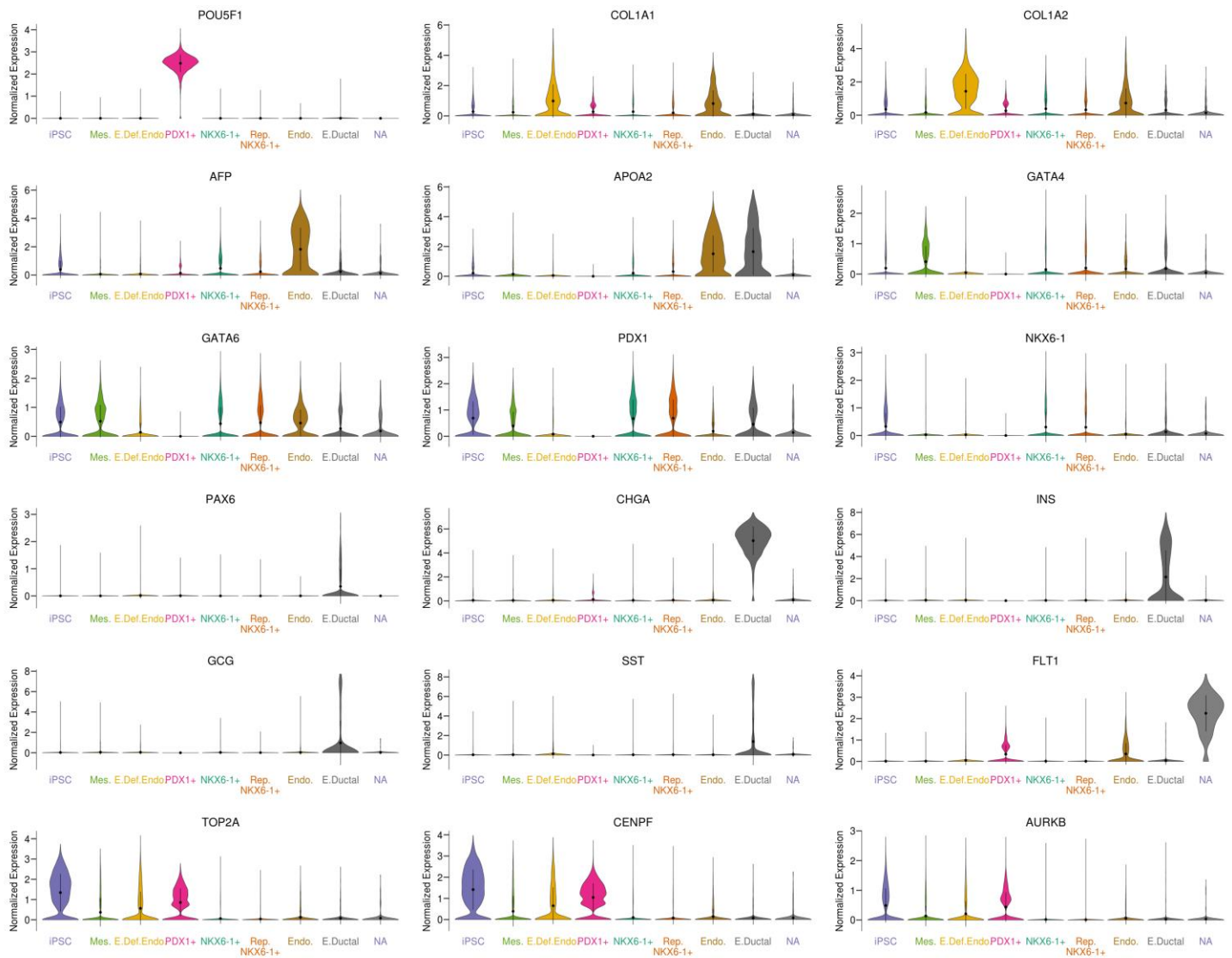
**Figure S4: Clustering of iPSC-PPC snATAC-seq at two additional resolutions**



We performed clustering analyses on 26,564 single nuclei from seven iPSC-PPC samples at resolutions 0.1 (shown in Figure 1D), 0.15 and 0.2. At resolutions 0.1, 0.15 and 0.20, we identified a total of five, six and seven clusters respectively. With increasing resolution, cluster 0 was further divided into subclusters that largely consist

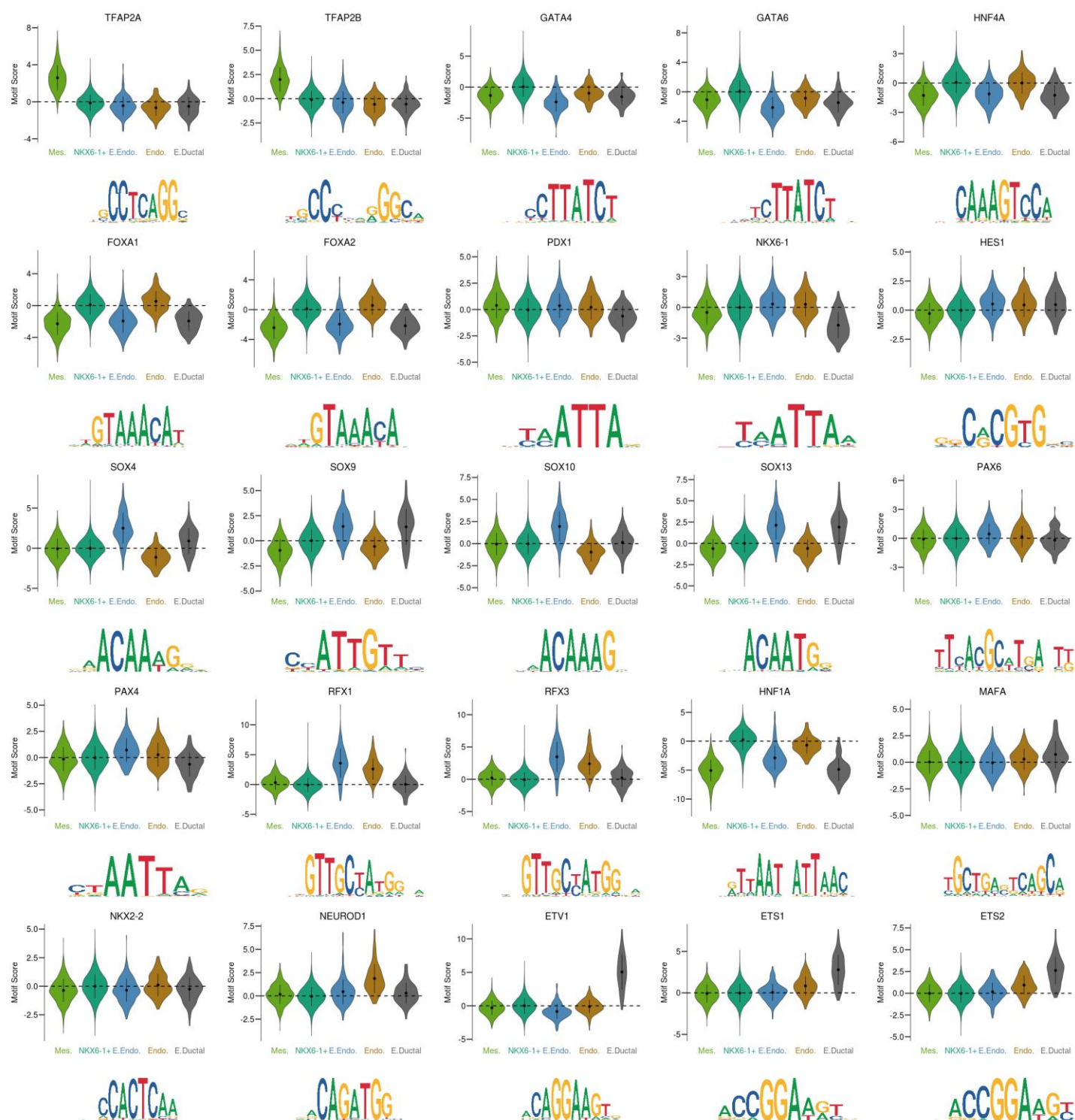
of *NKX6-1*<sup>+</sup> progenitors but with varying levels of PDX1 and NKX6-1 motif activities. Cluster labels in black correspond to clusters in snATAC-seq described in the UMAP plots above the heatmaps. Colored cluster labels correspond to iPSC-PPC scRNA-seq clusters described in Figure 1B. Red-to-blue shade in the heatmaps indicates Z-normalized expression for scRNA-seq or chromVAR motif activity for snATAC-seq.

### Figure S5: Expression of 17 marker genes in each of the eight scRNA-seq clusters



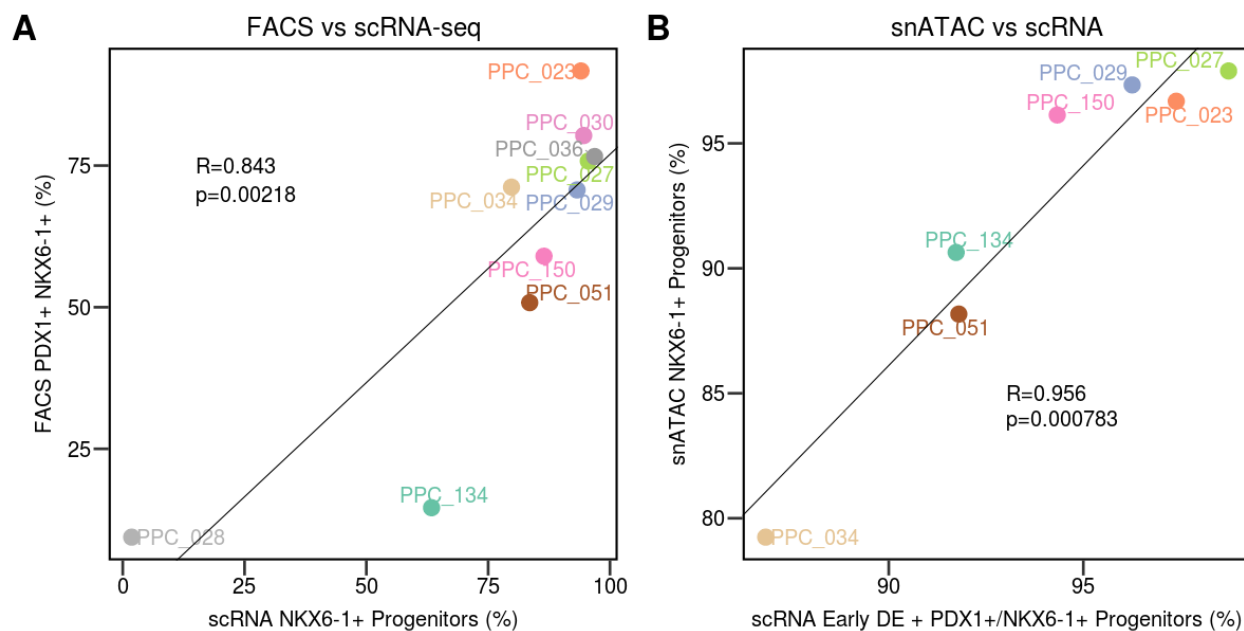
Violin plots showing the distributions of normalized expression for marker genes described in Figure 1F for each scRNA-seq cluster in Figure 1B.

**Figure S6: Motif activity of 23 transcription factors in each of the five snATAC-seq clusters**



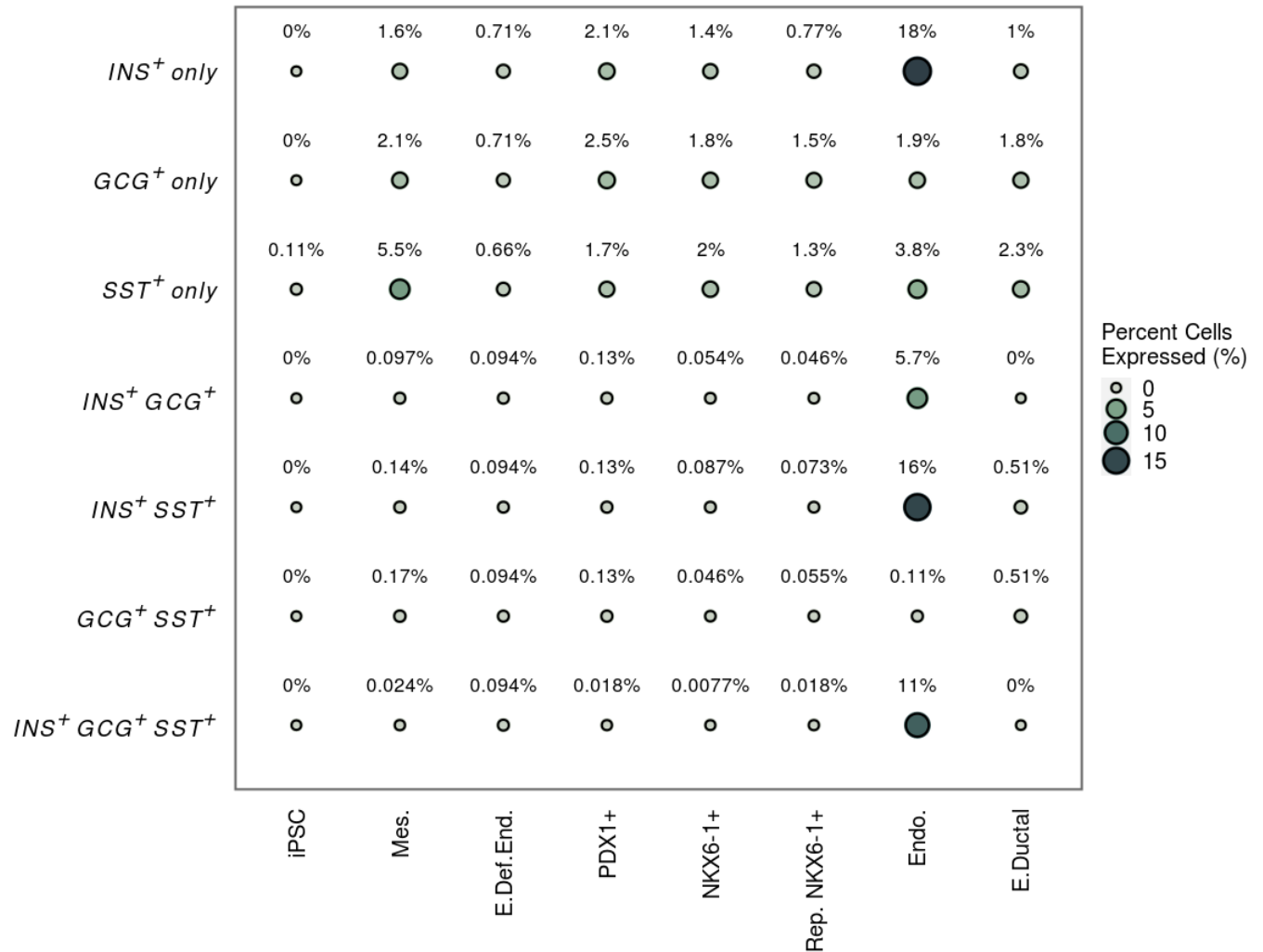
Violin plots showing the distribution of chromVAR motif activity score for the transcription factors described in Figure 1G for each snATAC-seq clusters in Figure 1D. Motif logos are shown underneath the corresponding plot.

**Figure S7: Correlation between flow cytometry, scRNA-seq and snATAC-seq results**



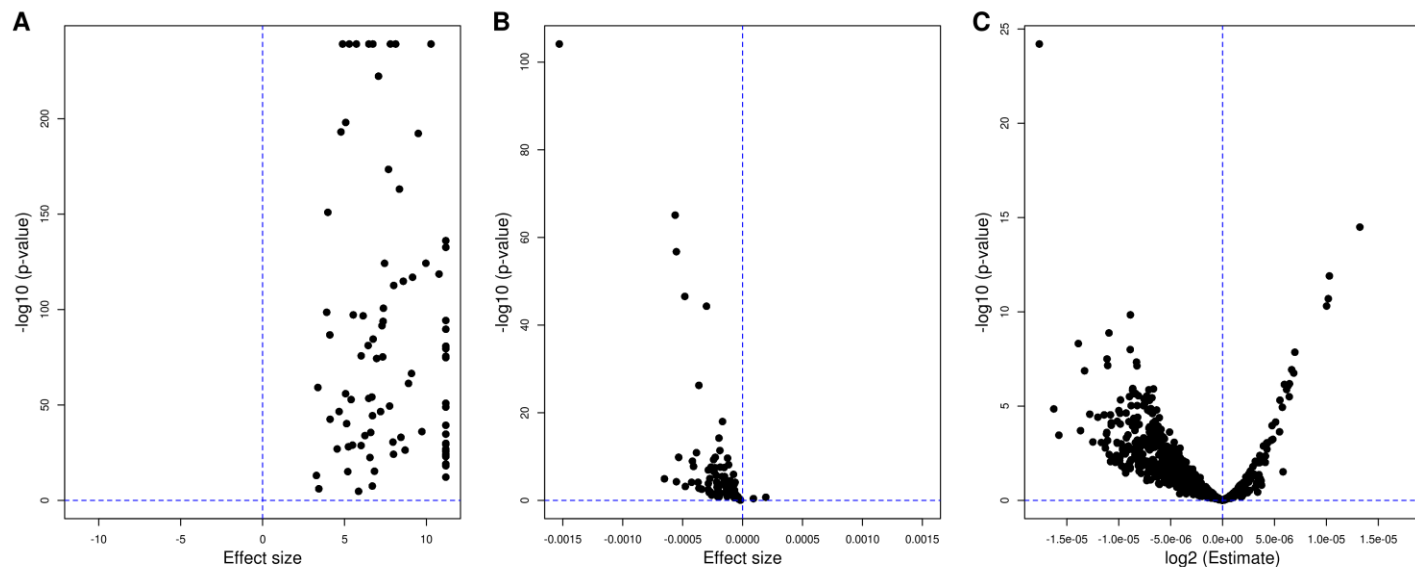
To determine the correspondence between FACS, scRNA-seq, and snATAC-seq, we compared the fraction of cells expressing both *PDX1* and *NKX6-1* within each iPSC-PPC sample. For scRNA-seq, we computed the total number of NKX6-1+ progenitors as the sum of NKX6-1+ progenitors and replicating NKX6-1+ progenitors (X axis, Figure S7A), as these cells express both *PDX1* and *NKX6-1*. We found that the FACS and scRNA-seq was significantly correlated ( $R = 0.843$ ,  $p = 0.00218$ , Figure S7A). We next determined whether the cell type fractions in snATAC-seq corresponds to scRNA-seq. Because snATAC-seq was not able to detect PDX1+ progenitors and early definitive endoderm (DE), we reasoned that these cells may be included in the main NKX6-1+ progenitor nuclei cluster. Therefore, we computed the fraction of cells that are early DE, PDX1+, NKX6-1+ progenitors and replicating NKX6-1+ progenitors in scRNA-seq and compared it to the fraction of nuclei that are NKX6-1+ progenitors in snATAC-seq. We found a significant correlation between scRNA-seq and snATAC-seq ( $R = 0.956$ ,  $p = 0.000783$ , Figure S7B). These results show that scRNA-seq, snATAC-seq, and FACs are highly associated with each other, and that both sequencing methods can capture the variable differentiation efficiency in iPSC-PPC.

**Figure S8: Co-expression of insulin, glucagon, and somatostatin in pancreatic progenitors**



Bubble plot showing the percentage of cells that express endocrine-specific hormones in scRNA-seq clusters, where radius and shade indicate the percentage of cells expressing above 10% of the maximal expression for the indicated gene across all cells.

### Figure S9: Associations between deltaSVM scores, ASE and transcription factor footprints



Volcano plots showing the associations between deltaSVM scores, ASE and transcription factor footprints. Each point represents a transcription factor.

(A) For each of the 89 transcription factors tested with both deltaSVM and TOBIAS, we investigated the agreement between these two tools. Here, we determined if variants predicted to have allelic effects on a specific transcription factor by deltaSVM were more likely than expected to occur at genomic locations bound to the same transcription factor, as determined by TOBIAS. Effect size (X axis,  $\log_2$  ratio) and p-values (Y axis, Fisher's exact tests) were measured using the *fisher.test* function in R. All tests had significant p-values after FDR correction (Benjamini-Hochberg) and had a positive  $\log_2$  ratio and, overall, the distribution of  $\log_2$  ratios was significantly greater than zero ( $p = 2.2 \times 10^{-47}$ , t-test, measured with the *t.test* function in R, with option *mu = 0*). Each dot represents one of the 89 tested transcription factors.

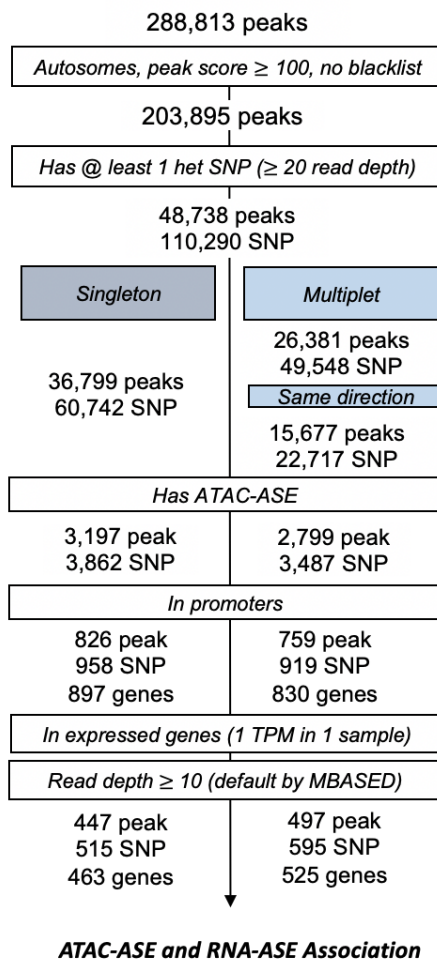
(B) For the same transcription factors in (A), we tested if variants predicted to have allelic effects by deltaSVM were more likely to be closer to transcription factor footprints determined using TOBIAS than expected. We computed the distance of each variant from the closest transcription factor footprint on the same peak, and performed a linear regression between the distance and the absolute value of the variant score measured by



deltaSVM. For all but two transcription factors, we observed a negative association (X axis = effect size; Y axis = p-value, measured using the *lm* function in R) and, overall, the effect size distribution was significantly lower than zero ( $p = 4.3 \times 10^{-15}$ , t-test, measured with the *t.test* function in R, with option  $mu = 0$ ), indicating that variants closer to transcription factor footprints are more likely to have stronger allelic effects.

(C) We tested the association between the major allelic frequency of each heterozygous variant in iPSC-PPC peaks tested for ASE and the distance from its closest footprint for each of the 746 transcription factors analyzed using TOBIAS. For most transcription factors, we observed a negative association (X axis = effect size; Y axis = p-value, measured using the *lm* function in R) and, overall, the effect size distribution was significantly lower than zero ( $p = 6.45 \times 10^{-84}$ , t-test, measured with the *t.test* function in R, with option  $mu = 0$ ), indicating that variants closer to transcription factor footprints are more likely to have stronger allelic effects.

## Figure S10: Workflow for computing allele-specific effects (ASE) in snATAC-seq peaks



Peaks on autosomal chromosomes were filtered based on: peak score  $\geq 100$ , not within ENCODE blacklist regions, and if they contained at least one heterozygous SNP in at least one of the seven snATAC-seq samples. SNPs were further categorized as singletons (i.e. observed in only one individual) or multiplets (i.e. observed in more than one individual). Multiplets with consistent allele direction in all individuals were retained. SNPs were then tested for ASE using a two-sided binomial test assuming a null hypothesis that both alleles were observed at equal proportions. We classified SNPs as having ASE if  $FDR \leq 0.05$  and major allele frequency  $\geq 0.6$ . SNPs with ASE at promoter regions were further examined for ASE association with gene expression using bulk RNA-seq (Figure 2D).

## TABLE LEGENDS

### **Table S1: Study information, including subject details, differentiation efficiency, and generated molecular data from 1 iPSC and 10 iPSC-PPCs**

In Sheet 1: Subject\_UUID is the assigned Universal Unique Identifier (UUID) for each subject (Column A) used in this study. Sex (Column B), age (Column C), and ethnicity (most similar 1KG population; Column D) are provided. iPSCORE\_Family (Column E) are the family identifiers used to identify related family members. Columns A-E are shown as included in dbGaP (phs001325.v1.p1; phs000924.v1.p1) as part of the iPSCORE Resource.

In Sheet 2: We provide information for each sample in our study. Subject\_UUID is provided in Column A. Cell\_type (Column B) indicates the type of cell (iPSC or PPC) obtained from each subject as part of this study. Unique Differentiation Identifier (UDID, Column C) is a unique digit assigned for each attempted iPSC-PPC differentiation. %PDX1+ (Column D), %NKX6.1+, (Column E), and %PDX1+\_NKX6.1+ (Column F) are the fractions of cells from each iPSC-PPC differentiation positively stained for PDX1, NKX6-1, or both PDX1 and NKX6-1, respectively. Data type indicates the type of sequencing method performed for each differentiation (Column G). The UUID for each sequenced sample is provided (Column H). Pooling schemes for samples combined prior to sequencing are shown (Column I).

In Sheet 3: We provide the UUIDs of each iPSC-PPC sample (Column A) by subject (Column B), WGS (Column C), bulk RNA-seq (Column D), fresh scRNA-seq (Column E), cryopreserved scRNA-seq (Column F), and snATAC-seq (Column G). Bulk RNA-seq was generated for all the of 10 iPSC-PPC samples that have scRNA-seq, but in this study we analyzed only the seven that have matched snATAC-seq (Table S1).

### **Table S2: scRNA-seq metadata**

The table shows, for each of the 83,971 single cells, the sample UDID (Column A), the preparation of the sample corresponding to either fresh or cryopreserved (Column B), the cell barcode (Column C), UUIDs for subject, WGS, and scRNA-seq (Columns D-F), the number of reads (Column G), the number of genes detected (Column H), the percent of mitochondrial reads (Column I), the cell type assignment (Column J), UMAP coordinates (Column K-L), and the cluster assignments at resolutions 0.05, 0.08, and 0.1 (Columns M-O). The UUIDs for WGS was obtained using Demuxlet (Kang et al., 2018) and then mapped to subject and sample UUID. Barcodes for cells from freshly prepared samples were formatted as *barcode-aggregate\_id* (Sheet 2) while those from cryopreserved samples were formatted as *barcode-1*.

Because this table's size is too large, it has been deposited on figshare:

<https://doi.org/10.6084/m9.figshare.15109581>

A Seurat R object including all scRNA-seq data has been deposited on figshare:

<https://doi.org/10.6084/m9.figshare.15109422>

### **Table S3: Genes differentially expressed in scRNA-seq clusters**

For each gene (Column A) and each scRNA-seq cluster (Column B), we computed Wilcoxon rank sum test between normalized expression values across cells within the cluster and cells outside of the cluster. The table provides the average log<sub>2</sub> fold-change between the groups (Column C), the average expression for each group (Column D-E), the fraction of cells with expression greater than 0.1 (Column F-G), the p-value (Column H), and q-value adjusted by Bonferroni correction (Column I). Genes with q-value  $\leq 0.05$  were considered differentially expressed.

### **Table S4: snATAC-seq metadata**

The table shows, for each of the 26,564 single nuclei, the cell barcode (Column A), the sample UDID (Column B), UUIDs for subject, WGS, snATAC-seq, and matched scRNA-seq (Columns C-F), quality control parameters

from CellRanger-ATAC and Signac (Columns G-V), the assigned cell type (Column W), UMAP coordinates (Column X-Y), and the cluster assignments at resolutions 0.1, 0.15, and 0.2 (Columns Z-AB). The UUIDs for WGS were obtained using Demuxlet (Kang et al., 2018) and then mapped to subject and sample UUID (snATAC-seq and scRNA-seq).

Because this table's size is too large, it has been deposited on figshare: <https://doi.org/10.6084/m9.figshare.15109581>

A Seurat R object including all snATAC-seq data has been deposited on figshare: <https://doi.org/10.6084/m9.figshare.15109422>

### **Table S5: Peaks differentially expressed in snATAC-seq**

For each cluster in snATAC-seq described in Figure 1D, we performed differential expression using the *FindAllMarkers* function in Signac. The table provides the cluster name, peak ID, average  $\log_2$  fold-change, the fraction of cells within cluster that has peak expression  $> 0.1$ , the fraction of cells outside of cluster that has peak expression  $> 0.1$ , p-value, and q-value adjusted with a Bonferroni correction. We consider peaks with q-value  $\leq 0.05$  to be differentially expressed.

### **Table S6: Motifs enriched in snATAC-seq peaks**

We performed motif enrichment analyses for 633 transcription factors in the JASPAR 2020 database. The table shows, for each snATAC-seq cluster, the tested motif ID and name from JASPAR, the p-value from Wilcoxon rank sum test, and the adjusted p-value using a Bonferroni correction. Motifs with q-value  $\leq 0.05$  were considered differentially enriched.

### **Table S7: Evidence of SNPs for association with transcription factor binding or allelic effects**

In total, we were able to investigate the functional associations for 349,572 variants, including 325,942 common SNPs (allele frequency > 5%) in the iPSCORE collection and 110,290 heterozygous variants in the seven iPSC-PPC samples (86,660 variants were in common). The table shows, for each variant, its associated peak, whether it belongs to the 325,942 common SNPs or to the 110,290 heterozygous variants and its functional associations: 1) overlap with transcription factor footprints (TOBIAS); 2) prediction of allele-specific effects (deltaSVM); or 3) ASE in snATAC-seq.

Because this table's size is too large, it has been deposited on figshare: <https://doi.org/10.6084/m9.figshare.15109581>

R objects including all results from TOBIAS, including the position of all bound transcription factor binding sites and all the overlaps between SNPs and transcription factor binding sites, have been deposited on figshare: A Seurat R object including all scRNA-seq data has been deposited on figshare: <https://doi.org/10.6084/m9.figshare.15109422>

### **Table S8: deltaSVM prediction of allele-specific transcription factor binding**

The table shows all associations between each of the 325,942 SNPs in snATAC-seq peaks and each of the 94 tested transcription factors. For each SNP, shown are: its chromosome and position, reference and alternative alleles, tested transcription factor, oligo binding score for reference and alternative allele (Yan et al., 2021), whether deltaSVM predicts that the transcription is bound, deltaSVM score for allelic TF binding, and the consequence of the SNP on the transcription factor binding (“Gain”: the alternative allele has a stronger binding score; “Loss”: the reference allele has a stronger binding score; “None”: no difference between reference and alternative alleles). Only the 52,653 SNPs predicted to be associated with allele-specific transcription factor binding are shown. A table including all 30,638,548 tested SNPs/transcription factor pairs has been deposited on Figshare (<https://doi.org/10.6084/m9.figshare.15109581>).

### **Table S9: Associations between transcription factor binding site predictions from deltaSVM and TOBIAS**

The table shows the enrichment for transcription factor binding and allelic effects predicted by deltaSVM in the genomic regions associated with a bound transcription factor annotated by TOBIAS. For each of the 89 transcription factors (the transcription factor ID by JASPAR and the transcription factor name by deltaSVM are shown in the table) in common between deltaSVM predictions and TOBIAS, we performed two enrichment analyses (shown in Figure S9A,B): 1) we tested for the enrichment of variants predicted to overlap a transcription factor binding site by deltaSVM and bound transcription factor binding sites measured by TOBIAS, using Fisher's exact test (the table shows estimate, p-value and q-value adjusted using Benjamini-Hochberg's method); and 2) we tested for the enrichment of variants predicted by deltaSVM to have allelic effects at a transcription factor binding site and bound transcription factor sites measured by TOBIAS, using linear regression (the table shows effect size, standard error, p-value and q-value adjusted using Benjamini-Hochberg's method).

### **Table S10: Allele-specific effects of heterozygous SNPs in snATAC-seq peaks**

Shown are the allele-specific effects of heterozygous SNPs with read depth  $\geq 20$  in heterozygous iPSCORE individuals (Column A). Variant ID indicates the chromosome position, reference allele, and alternate allele of the heterozygous SNP (Column B). The peak that overlaps with the SNP (Column C), the peak score from MACS2 (Column D) and the gene ID and name whose promoter overlaps with the SNP (Column E-F) are provided. The number of reads calculated by *samtools mpileup* from snATAC-seq BAM files overlapping the reference allele, alternative allele, or both are shown (Columns G-I). The major allele frequency was calculated as the fraction of reads that map to the allele with greater number of reads (Column J). Information about whether the variant is a singleton (i.e. observed only in one individual) (Column K) or observed in a single allele direction are given (Column K-L). P-values (Column M) were calculated using binomial test with the alternative hypothesis that both alleles were observed in equal frequency. P-values were adjusted using Benjamini-Hochberg's method (Column N). SNPs showed allele-specific effects if  $FDR \leq 0.05$  and the major allele frequency is  $\geq 0.6$  (Column O).

Because this table's size is too large, it has been deposited on figshare:

<https://doi.org/10.6084/m9.figshare.15109581>

### **Table S11: deltaSVM prediction of allele-specific transcription factor binding**

The table shows the associations between deltaSVM scores and the alternative allele frequency of all SNPs overlapping bound transcription factors. Shown are: the SNP ID (as in Table S4), transcription factor, deltaSVM score and allele frequency calculated from snATAC-seq.

Because this table's size is too large, it has been deposited on figshare:

<https://doi.org/10.6084/m9.figshare.15109581>.

### **Table S12: Associations between transcription factor binding and ASE**

The table shows the associations between the major allele frequency of variant tested for ASE and its distance from each bound transcription factor binding site in the same snATAC-seq peak measured by TOBIAS (Figure S9C). The table shows, for each of the tested 746 transcription factors, its JASPAR ID, the measured effect size, standard error, p-value and q-value adjusted using Benjamini-Hochberg's method.

### **Table S13: Correspondence between ASE at promoters and their associated genes**

Shown are the allele-specific effects of 5,380 expressed genes that have a snATAC-seq peak at the promoter region. The analysis was performed using MBASED (Mayba et al., 2014) on a per-sample basis. For each sample and gene (Columns A-C), we provide information about the major allele frequency (Column D), p-value of heterogeneity (Column E), p-value of ASE (Column F), FDR-corrected p-value using Benjamini Hochberg's method (Column G), and whether this gene exhibits ASE or not (Column H). We determine a gene to exhibit ASE if  $FDR \leq 0.05$  and the major allele frequency is  $\geq 0.6$ . The major allele frequency, p-value of ASE, and p-value of heterogeneity were computed by MBASED using the 1-sample analysis in the provided protocol.



### **Table S14: Associations between T2D-associated SNPs and allelic effects in iPSC-PPC**

For each of the 66,600 SNPs in T2D credible sets (Mahajan et al., 2018), the table shows: their associated locus, including the position of the index SNP, the index gene and the RS ID of the index SNP, as defined in Mahajan et al. (Mahajan et al., 2018); the PPA and the rank in the credible set; whether each SNP overlaps an iPSC-PPC snATAC-seq peak; whether it is predicted to have allelic effects, based on deltaSVM results; and whether it has ASE in the iPSC-PPC snATAC-seq dataset.

## References

- DeBoever, C., Li, H., Jakubosky, D., Benaglio, P., Reyna, J., Olson, K.M., Huang, H., Biggs, W., Sandoval, E., D'Antonio, M., *et al.* (2017). Large-Scale Profiling Reveals the Influence of Genetic Variation on Gene Expression in Human Induced Pluripotent Stem Cells. *Cell Stem Cell* 20, 533-546 e537.
- Kang, H.M., Subramaniam, M., Targ, S., Nguyen, M., Maliskova, L., McCarthy, E., Wan, E., Wong, S., Byrnes, L., Lanata, C.M., *et al.* (2018). Multiplexed droplet single-cell RNA-sequencing using natural genetic variation. *Nat Biotechnol* 36, 89-94.
- Mahajan, A., Taliun, D., Thurner, M., Robertson, N.R., Torres, J.M., Rayner, N.W., Payne, A.J., Steinhorsdottir, V., Scott, R.A., Grarup, N., *et al.* (2018). Fine-mapping type 2 diabetes loci to single-variant resolution using high-density imputation and islet-specific epigenome maps. *Nat Genet* 50, 1505-1513.
- Mayba, O., Gilbert, H.N., Liu, J., Haverty, P.M., Jhunjhunwala, S., Jiang, Z., Watanabe, C., and Zhang, Z. (2014). MBASED: allele-specific expression detection in cancer tissues and cell lines. *Genome Biol* 15, 405.
- Veres, A., Faust, A.L., Bushnell, H.L., Engquist, E.N., Kenty, J.H., Harb, G., Poh, Y.C., Sintov, E., Gurtler, M., Pagliuca, F.W., *et al.* (2019). Charting cellular identity during human in vitro beta-cell differentiation. *Nature* 569, 368-373.
- Yan, J., Qiu, Y., Ribeiro Dos Santos, A.M., Yin, Y., Li, Y.E., Vinckier, N., Nariai, N., Benaglio, P., Raman, A., Li, X., *et al.* (2021). Systematic analysis of binding of transcription factors to noncoding variants. *Nature* 591, 147-151.